To the Graduate Council:

I am submitting herewith a dissertation written by Robert Timothy Short entitled "Recoil-Energy Measurements of Slow Highly-Charged Ions Produced by Synchrotron Radiation and by Swift-Ion Impact." I have examined the final copy of this dissertation for form and content and recommend that it be accepted in partial fulfillment of the requirements for the degree of Doctor of Philosophy, with a major in Physics.

Ivan A. Sellin, Major Professor

We have read this dissertation
and recommend its acceptance:

Accepted for the Council:

Vice Provost
and Dean of The Graduate School

RECOIL-ENERGY MEASUREMENTS OF SLOW HIGHLY-CHARGED IONS PRODUCED BY SYNCHROTRON RADIATION AND BY SWIFT-ION IMPACT

A Dissertation

Presented for the

Doctor of Philosophy

Degree

The University of Tennessee, Knoxville

Robert Timothy Short

June 1987

ACKNOWLEDGEMENTS

In the course of dissertation research, a number of people have assisted me generously. I am particularly indebted to Dr. Ivan Sellin, my major professor, whose foresight and unparalleled enthusiasm made this work possible. His insight was also quite useful at troubling stages of data analysis. The close guidance of Dr. Chun-Sing O during my training in experimental research is greatly appreciated. His help in preparation for experiments, especially for those at synchrotron radiation laboratories, was invaluable. Dr. Jon Levin contributed immeasurably in the course of this work through his expertise in synchrotron radiation and data analysis, and I am certainly in his debt. I gratefully acknowledge the frequent consultation of Dr. Marianne Breinig, Dr. Joachim Burdörfer, Dr. Robert DeSerio, and Dr. Stuart Elston, as well as the help of other members of the UT Atomic Physics group during experimental runs.

I thank our Swedish collaborators, Dr. Leif Liljeby, Dr. Sven Huldt, Dr. Sveneric Johansson, Dr. Henrik Cederquist, and Elisabeth Nilsson for their significant contributions during experiments at the Stanford Synchrotron Radiation Laboratory. I also am grateful to Hans-Peter Hülskötter for his permission to include pages from his Diplomarbeit as an appendix to this work.

Finally, I would like to express my sincere thanks to my wife, Teresa, for her patience and understanding during my long absences from home. Her continued support and encouragement certainly contributed to my success and enjoyment during my years in graduate school.

ABSTRACT

A novel time-of-flight technique was used to measure average energies of ions produced by inner-shell photoionization of inert-gas atoms with synchrotron radiation in order to investigate the feasibility of developing a Very Cold Ion Source (VCIS). Multiply-charged Ne, Ar, Kr, and Xe ions were produced in vacancy cascades following inner-shell photoionization by x rays from a wiggler line at Stanford Synchrotron Radiation Laboratory, and the resulting charge-state distributions and average kinetic energies were measured using a time-of-flight spectrometer. Ion energies were found to correspond essentially to room temperature, and observed ion intensities show promise for future use in very-low-energy atomic collisions and precision spectroscopy studies.

Recoil energies were similarly measured for Ne and Ar ions produced by swift-ion impact using the EN Tandem accelerator at Oak Ridge National Laboratory. Average energies for the higher charge states were found to be up to 2 orders of magnitude larger than for those produced by photoionization. Impact parameters important in the collision processes were inferred from measured recoil energies using a screened-Coulomb scattering model. Knowledge of recoil-ion energies may be useful for the future development of parasitic low-energy ion sources on heavy-ion accelerators.

TABLE OF CONTENTS

CHAPTER		PAGE
1.	INTRODUCTION	1
2.	REVIEW OF MULTIPLE IONIZATION	5
	Inner-Shell Photoionization	5
	Swift Ion Impact	10
3.	EXPERIMENTAL METHOD	16
	Time-of-Flight Technique	16
	Time-of-Flight Spectrometer	20
	Stanford Synchrotron Radiation Laboratory Setup	28
	Oak Ridge National Laboratory Setup	36
4.	DATA ANALYSIS	46
	Fitting of Raw Spectra	46
	Determination of Recoil Energy	56
5.	RESULTS AND DISCUSSION	64
	Inner-Shell Photoionization (SSRL)	64
	Swift-Ion Impact (ORNL)	70
6.	SUMMARY	83
LIST OF REFERENCES		86
APPENDICES		92
APPENDIX A.	DERIVATION OF FLIGHT TIME EQUATIONS	92
APPENDIX B.	PPAD AND BEAM CHARGE STATE ANALYSIS SYSTEM	96
VITA		102

LIST OF TABLES

TABLE		PAGE
3.1.	Critical Dimensions of TOF Spectrometer	22
3.2.	Calculated Flight Times for Ar^{4+} Ions in TOF Spectrometer Using Nominal Optimum Electric Field Values	26
3.3.	TOF Spectrometer Operating Parameters at SSRL	35
3.4.	TOF Spectrometer Operating Parameters at ORNL	45
3.5.	Voltages for Electron MCP Detector at ORNL	45
4.1.	Linear (β) Terms Obtained from Quadratic Fits of TOF Peak Widths for Ions Produced by Inner-Shell Photoionization	59
4.2.	Average Linear (β) Terms Used for Quadratic Fits of TOF Peak Widths for Recoil Ions Produced by Swift-Ion Impact	63
5.1.	Measured and Estimated Average Energies ($\bar{U}_o$) of Inert Gases Following Inner-Shell Photoionization with Broad Spectrum Synchrotron Radiation	64
5.2.	Charge State Fractions Observed Following Inner-Shell Photoionization of Inert-Gas Atoms with Broad Spectrum Synchrotron Radiation	67
5.3.	Average Charge States ($\bar{q}$) Observed Following Inner-Shell Photoionization of Inert-Gas Atoms	69
5.4.	Average Recoil-Ion Energies ($\bar{E}_R$) of Neon and Argon Ions Produced in Collisions of Fast Chlorine Ions with Dilute Gas Targets	71
5.5.	Average Energies ($\bar{E}_R$) and Impact Parameters ($\bar{b}$) for Neon and Argon Recoil Ions Detected in Coincidence with Exiting Projectile Ions Cl^{r+}	78

LIST OF FIGURES

FIGURE		PAGE
2.1.	Schematic Representation of a Vacancy Cascade in Xe . .	7
3.1.	Schematic of a Two-Stage TOF Spectrometer	17
3.2.	TOF Spectrometer of Wiley and McLaren Design	19
3.3.	TOF Spectrometer used in Present Experiments	21
3.4.	Schematic of the SSRL Beamline and TOF Experiment Chamber	29
3.5.	SPEAR Bending Magnet and SSRL Wiggler Spectra for Various Stored Electron Energies, E_e	30
3.6.	Schematic of Ion TOF apparatus at SSRL	33
3.7.	Schematic of ORNL Beamline and Recoil-ion TOF Experiment Chamber	37
3.8.	Electron Detection Schematic	39
3.9.	Schematic of TOF Apparatus for Coincident Electron and Recoil-Ion Detection at ORNL	41
3.10.	Schematic of TOF Apparatus for Coincident Projectile and Recoil-Ion Detection at ORNL	42
4.1.	Neon TOF Spectrum Displaying Charge-State Distribution Resulting from Production of Single K-Shell Vacancies	47
4.2.	Argon TOF Spectrum Displaying Charge-State Distribution Resulting from Production of Single K-Shell Vacancies	47
4.3.	Krypton TOF Spectrum Displaying Charge-State Distribution Resulting from Production of Single L-Shell Vacancies	48
4.4.	Xenon TOF Spectrum Displaying Charge-State Distribution Resulting from Production of Single M- and L-Shell Vacancies	48
4.5.	Peaks from TOF Spectra Obtained at SSRL which Display Mass Isotope Resolution	49

FIGURE PAGE

4.6. Ar^{4+} TOF Peaks Obtained using Scaled Spectrometer Electric Fields Corresponding to κ = 1 1/2, 1/4, and 1/8 51

4.7. Neon Recoil-Ion Charge-State Distribution Created by an Incident 22.5 MeV Cl^{4+} Beam and Observed in Coincidence with Electrons Ejected During Ionization 52

4.8. Argon Recoil-Ion Charge-State Distribution Created by an Incident 23 MeV Cl^{5+} Beam and Observed in Coincidence with Electrons Ejected During Ionization 52

4.9. Argon Recoil-Ion Charge-State Distributions Created by an Incident 23 MeV Cl^{5+} Beam and Observed in Coincidence with Exiting Projectile Charge-State 54

4.10. Dependence of TOF Peak Width on Spectrometer Electric Field Scaling Parameter (κ) for Electrons Detected in Coincidence with Projectile Ions 55

4.11. Quadratic Fits of TOF Peak Widths Used to Determine Recoil Energies of Neon, Argon, Krypton, and Xenon Ions Produced by Inner-Shell Photoionization 58

4.12. Quadratic Fits of TOF Peak Widths Used to Determine Recoil Energies of Argon Ions Produced by an Incident 23 MeV Cl^{5+} Beam and Detected in Coincidence with Electrons 60

4.13. Quadratic Fits of TOF Peak Widths Used to Determine Recoil Energies of Neon Ions Produced by an Incident 22.5 MeV Cl^{4+} Beam and Detected in Coincidence with Scattered Cl^{8+} Projectile Ions 61

4.14. Quadratic Fits of TOF Peak Widths Used to Determine Recoil Energies of Argon Ions Produced by an Incident 23 MeV Cl^{5+} Beam and Detected in Coincidence with Scattered Cl^{8+} Projectile Ions 61

5.1. Average Recoil Energies ($\bar{E}_R$) of Argon Ions Produced by 18, 23, 27.6, and 33 MeV Cl^{5+} Ions Plotted vs. Recoil-Ion Charge State 72

5.2. Average Recoil Energies ($\bar{E}_R$) of Neon Ions Produced by 22.5 MeV Cl^{4+} Ions and Detected in Coincidence with Exiting Projectile-Ion Charge States 74

FIGURE PAGE

5.3. Average Recoil Energies ($\bar{E}_R$) of Argon Ions Produced by 23 MeV Cl^{5+} Ions and Detected in Coincidence with Exiting Projectile-Ion Charge States 74

5.4. Ar^{9+} Recoil Energies as a Function of Impact Parameter for 23 MeV $Cl^{5+} + Ar \rightarrow Cl^{8+} + Ar^{9+}$ for the Present Calculation, a CTMC Model, and Bohr Screening 76

5.5. Argon Recoil Energy ($\bar{E}_R$) vs. Product (pq) of Incoming Projectile Charge and Recoil-Ion Charge for Beams of 18, 23, 27.6, and 33 MeV Cl^{5+} 79

5.6. Argon Recoil Energy ($\bar{E}_R$) vs. Product (rq) of Final Projectile Charge and Recoil-Ion Charge for Beams of 23, 27.6, and 33 MeV Cl^{5} 80

5.7. Recoil-Ion Energy ($\bar{E}_R$) vs. Reaction Energy (Q) for Beams of 22.5 MeV Cl^{4+} Incident on Neon, and 23, 27.6 MeV Cl^{5+} Incident on Argon 82

CHAPTER 1

INTRODUCTION

Research activity concerning the physics of highly-ionized systems has grown quite rapidly during the past two decades. In particular, properties of slow highly-charged ions have been the topic of numerous recent studies (Chapter 2). Some of the most abundant forms of matter in the universe exist inside stars in states of high ionization and excitation, and the atomic processes involving highly-charged ions, which are fundamental in the static and dynamic behavior of stellar atmospheres, are far from being fully understood. Furthermore, measurements of binding energies (or Lamb shifts) of very tightly bound electrons in slow, one-electron, high-Z ions could provide a critical test of QED and relativistic effects in atomic structure, since the accuracy of fast-beam spectroscopic techniques is inherently limited by Doppler spreads.

Understanding of the structure and reaction mechanisms of high charge-state ions is, however, not only of intrinsic scientific interest, but of great practical interest as well. Radiative energy loss due to electron capture and excitation mechanisms involving slow highly-charged impurity ions is a significant problem in tokamak fusion plasmas. In addition, stimulated emission induced by laser pumping of metastable states of high charge state ions may be possible, leading to the development of x-ray and VUV laser systems. The many recent international conferences concerning high-charge-state ion structure and collision phenomena are evidence of the widespread and rapidly

growing interest in this field, including conferences held in Lyon (1978), Stockholm (1982), Oxford (1984), and Groeningen (1986).

Unfortunately, sources of highly-charged ions are not readily available under desirable experimental conditions. In plasmas, where states of high ionization are common, high temperatures and densities make sensitive atomic measurements very difficult. For example, effective temperatures in laser produced plasmas can reach hundreds of kilovolts. Doppler broadening of spectral lines resulting from such a distribution of energetic ions severely limits the accuracy of atomic structure measurements made under these conditions. Information concerning atomic collisions is also difficult to obtain due to multiple collisions resulting from the high number densities of ions found in plasmas.

Heavy funding has been devoted worldwide to the development of high-flux ion sources, such as cryogenic electron beam ion sources (CRYEBIS) and electron cyclotron resonance ion sources (ECRIS). Storage rings for cooled heavy ions have been proposed or are under construction at several facilities around the globe--for example, HISTRAP at Oak Ridge National Laboratory, CRYRING at AFI in Stockholm, TSR at the Physikalisches Institut in Heidelberg, and ESR at GSI in Darmstadt. In conjunction with these projects, various schemes for cooling ions to low temperatures have been proposed. Electron beam cooling is chief among these, and cooling stages of this type are planned for most of the storage rings mentioned above.

Since schemes to cool ions to low temperatures would become more feasible if a room temperature ion source were available, the possibility of creating cold highly-charged ions by photoionizing inner-shells of inert-gas atoms with synchrotron radiation was investigated. Intense x-ray beams from the Stanford Synchrotron Radiation Laboratory were used to photoionize atomic inner-shells in dilute inert gas samples. Average kinetic (i.e., recoil) energies of the resulting neon, argon, krypton, and xenon ions were measured using a novel time-of-flight (TOF) technique; charge-state distributions of each gas were also determined by TOF methods. The incident photon impact and subsequent readjustments to the inner-shell vacancies were found to transfer very little kinetic energy to the target nuclei. The measured ion energies corresponded essentially to room temperature (even for high charge states) and intensities were sufficiently high to be promising for future low-energy collision and precision spectroscopy experiments.

In order to compare recoil energies of ions produced by inner-shell photoionization with those of ions produced by swift ion impact, average recoil energies of neon and argon ions created in collisions of ~0.5 - 1 MeV/u Cl^{p+} (p=4,5) ions with dilute gas targets were similarly measured at the Oak Ridge National Laboratory EN Tandem Van deGraaff accelerator facility. Recoil energies of the higher charge state ions produced in this manner were up to two orders of magnitude greater than those of ions produced by synchrotron radiation inner-shell photoionization. A steep dependence of recoil energy on exiting charge state of both projectile and target was observed. It

was then possible to characterize impact parameters important in the creation of these ions by comparing the measurements to results calculated using a screened-Coulomb scattering model of the collision process, in conjunction with two-body energy-momentum conservation.

These measurements improve on earlier estimates and upper limits of recoil-ion energies. They not only provide insight into ion-atom collision mechanisms at high velocities, but may also be useful in the design of parasitic low-energy ion sources on heavy-ion accelerators.

CHAPTER 2

REVIEW OF MULTIPLE IONIZATION

Inner-Shell Photoionization

Around twenty years ago, Carlson and collaborators (Carlson et al., 1966) studied multiple ionization resulting from inner-shell vacancy production in inert-gas atoms in great detail. They measured ion charge-state distributions by magnetic analysis following photoionization of various shells in neon (Krause et al., 1964), argon (Carlson and Krause, 1965), krypton (Krause and Carlson, 1967), and xenon (Carlson et al., 1966). Standard low intensity x-ray-tube sources and filters provided the low intensity beams of x rays used for photoionization within each atomic shell. Fairly good agreement was found between their experimental results and theoretical distributions they derived from Monte Carlo calculations modeling the radiative and nonradiative electronic readjustment to inner-shell vacancies. They even devised a simple recipe to estimate the average charge state resulting from an inner-shell vacancy in any atom in the periodic table (Carlson et al., 1966).

A few years later, Lightner et al. (1971) used a time-of-flight spectrometer to measure abundances of multiply-charged neon, argon, and krypton ions produced by photoionization with x rays from low-intensity x-ray tube sources, and found distributions essentially consistent with those of Carlson and co-workers. They were able to explain some discrepancies between theory and experiment by including electron correlation effects in the description of the ionization process and by

considering the energy dependence of partial photoionization cross sections (Rakavy and Ron, 1967).

The two major processes leading to multiple ionization following creation of a single inner-shell vacancy were discussed quite thoroughly by Carlson (1975a) and are worthy of review here; these are vacancy cascades and electron shake-off.

When a vacancy is produced in an inner shell of an atom, it is filled by either a radiative (x ray) or nonradiative (Auger) transition. In an Auger transition, the vacancy is filled by an electron from a higher shell, or even the same shell (Coster-Kronig transition) when energetically possible, while another electron is simultaneously ejected into the continuum. The Auger process dominates in all cases, except for vacancies in the K-shells of atoms with $Z > 30$ and some L-shells of very heavy elements. Vacancy cascades are a series of discrete Auger processes that can occur as a result of one initial inner-shell vacancy. These cascades are best illustrated by an example (Figure 2.1) which shows a possible vacancy cascade following L-shell vacancy production in xenon. The initial Auger transition leaves two vacancies in the M-shell, which are each filled by Auger transitions from the N-shell. The N-shell vacancies are then filled through Auger, Coster-Kronig, and radiative transitions, creating a xenon ion of charge eight. Vacancy cascades take place very quickly, typically within a time scale of 10^{-14} to 10^{-15} seconds, and result in a charge-state distribution of ions which is statistically determined by branching ratios and decay rates. In order to explain experimental

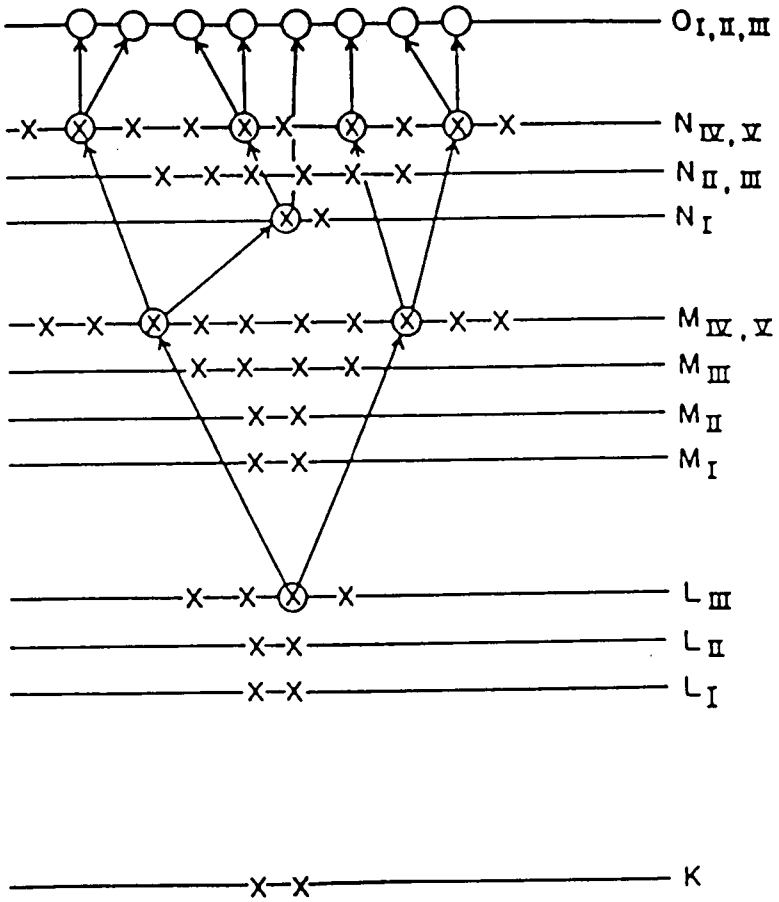


Figure 2.1. Schematic representation of a vacancy cascade in Xe. X , electrons; ○, vacancies; ⊗, vacancies that were subsequently filled by electrons.

Source: after T. A. Carlson, 1975, Photoelectron and Auger Spectroscopy, (Plenum, New York).

distributions observed, however, electron shake-off effects must also be included.

Electron shake-off is caused by a sudden change in the central atomic potential. When an inner-shell electron is ejected, a change in the atomic central potential is felt by electrons in outer shells, since the removal of an electron reduces the effective screening of the nuclear charge for the remaining electrons. This sudden potential change can result in an atomic electron being found in an excited state (electron shake-up) or in the continuum (electron shake-off). The probability (P_{nlj}) for these processes can be calculated, using the sudden approximation (Carlson and Nestor, 1973), by finding the probability that each electron will remain in its initial orbital, and subtracting from one

$$P_{nlj} = 1 - \left[\left|\int \psi^*_{nlj}(A_i)\psi_{nlj}(A_o)dr\right|^2\right]^N - P_f. \qquad (2.1)$$

The exponent N is the number of electrons in orbital nlj, and the bracketed portion of Equation 2.1 determines the square of the overlap integral of the initial state A_o (prior to the ionization event) and final state A_i (after primary ionization event) wave functions. A small correction (P_f) must be subtracted to account for the Pauli exclusion principle--excitation to occupied states is forbidden. Since the final state wave functions are not eigenstates of the initial neutral atom, there is a finite probability that an electron will be found in a continuum state of the ion created by the primary ionization event.

Investigations of inner-shell processes and related phenomena have greatly benefited from the advent of synchrotron radiation laboratories. Synchrotron radiation was first considered to be only an annoying energy-loss mechanism in circular electron accelerators and storage rings; it was later demonstrated to be a useful photon source. The availability of high intensity and well collimated beams of continuous radiation (VUV to hard x-ray) from electron storage rings has stimulated research in many areas of solid state and atomic physics that were previously not feasible. A series of articles in Physics Today (Bienenstock and Winick, 1983; Mills, 1984; Crasemann and Wuilleumier, 1984) review many of the recent research efforts involving synchrotron radiation.

Hastings and Kostroun (1983) used monochromatic x rays from the CHESS synchrotron-radiation facility at Cornell University to photoionize inner-shells in krypton. A time-of-flight spectrometer was used to measure the charge-state distributions of krypton ions following photoionization at x-ray energies just below, at the peak, and just above the K-shell ionization threshold, in order to investigate photon absorption near threshold. The charge-state distribution was peaked at a higher charge state when K-shell ionization was energetically possible.

Calculations based on the design parameters for the National Synchrotron Light Source (NSLS) at Brookhaven National Laboratory led Jones, Johnson, and Meron (1983) to postulate the feasibility of a PHOton Beam Ion Source (PHOBIS). They proposed trapping source ions in a potential well (e.g., Kingdon trap) in the path of an intense photon

beam. High states of ionization would be produced by successive stripping of electrons, since the spectral distribution of synchrotron radiation is continuous. They predicted that completely stripped ions could be produced on a time scale of several seconds, however, no experimental evidence exists at this time. Similarly, Church et al. (1984) proposed producing and storing highly-charged ions at room temperature in a Penning ion trap at NSLS. Experimental investigations have begun, and publication of initial results are expected (Church, 1987). The present results established the feasibility of the x-ray pumping portion of the proposed ion-trapping scheme.

Swift Ion Impact

During the late 1960's and early 1970's, accelerator beams were found to provide a very clean source of highly ionized and excited atomic systems. After passing through thin solid or gaseous targets, fast heavy ions are left in states of high excitation and ionization that are easily studied, since the beams are typically well collimated, their energies well defined, and they emerge into high vacuum. Beam-foil spectroscopy has yielded much important data concerning high-charge-state ion structure and collision phenomena (Sellin and Pegg, 1975). However, spectroscopic measurements made in this manner are intrinsically limited (Bashkin, 1968) by the Doppler shifts and spreads resulting from the fast beam velocities.

More recently, multiply-charged recoil ions produced in collisions of fast heavy ion beams with neutral gas targets have been the objects of study. Richard et al. (1969) first noticed that multiply-charged nickel and copper ions were produced in collisions of oxygen beams with

gas targets by measuring a shift in the nickel and copper K_β x-ray energies. Mowat et al. (1973) and Brown et al. (1974) later observed similar shifts in K x-ray energies from multiply-ionized neon and argon recoil ions. However, Sellin et al., (1977) introduced the field of recoil ion spectroscopy by demonstrating that recoil ions are produced in very-high states of ionization (e.g., up to hydrogen-like neon) at high rates (cross sections $\sim 10^{-18}$ cm^2 for Ne^{7+}), and that they have low recoil velocities (estimated at $\sim 10^{-5}c$), thus possibly permitting significantly higher resolution spectroscopy than possible with beam-foil methods. Since then, ultraviolet transitions in helium-like neon recoils (Klein et al., 1982) and x-ray transitions in helium-like argon recoils (Deslattes et al., 1984) have been observed. More recently, Beyer et al. (1985) were able to determine the 1s Lamb shift to 1.5% in slow hydrogen-like argon recoil ions produced by highly-stripped energetic uranium ions.

Numerous recoil-ion production cross section measurements have been made in order to better understand the collision mechanisms leading to multiple ionization, as well as to investigate the practicality of using these recoil ions for further study. Cocke (1979) presented the first systematic set of cross section measurements for recoil ion production, in which he investigated cross section dependence on incident projectile energy and charge. He used a time-of-flight spectrometer to determine the charge states of slow helium, neon, and argon ions generated in collisions of 25-45 MeV chlorine ions with neutral gas targets, and also obtained crude upper limits for recoil- ion energies (e.g., 5 eV for Ne^{2+}, and 30 eV for Ne^{7+}) from the

widths of the time-of-flight peaks. Production cross sections were found to peak for charge-state-one recoil ions and decrease with increasing charge state. Haugen et al. (1982) also determined absolute ionization cross sections for interactions of numerous MeV bare projectile ions and inert-gas atoms. Studies of symmetric collisions of ~1 MeV/u argon ions and neutral argon atoms (Tonuma et al., 1984) showed a dramatic shift to higher recoil-ion charge states when projectile ions had L-shell vacancies, indicating possible direct transfer of target L-shell electrons to projectile ions. Measurements in which final charge states of projectile ions were detected in coincidence with recoil ion production (Gray et al., 1980; Muller et al., 1986) also showed shifts to higher recoil-ion charge states when multiple projectile ionization or electron capture occurred, and have given insight into multiple ionization and capture phenomena at high velocities.

Two classes of theoretical models have typically been used to calculate cross sections for recoil ion production. These are the energy deposition (ED) model developed by Russek and collaborators (Russek, 1963; and references therein), and the independent particle (IP) model developed by Hansteen and Mosebekk (1972), and McGuire and Weaver (1977). In the ED model, multiple ionization is deemed to occur in two steps: (1) part of the translational energy of the projectile is deposited as electronic excitation in the collision partners; (2) after the partners separate, excess electronic energy in each partner is redistributed among the electrons, and each system autoionizes to reach its final ionization state. In the IP model, collision times are

assumed to be sufficiently short compared to the characteristic orbital times of outer-shell electrons, allowing the fate of each electron to be treated independently of all others. The impact parameter-dependent probability $P_n(b)$ for ejection of n electrons can then be found by binomial statistics.

Olson (1979) used the IP model in classical-trajectory Monte Carlo (CTMC) calculations of multiple-ionization cross sections for 1-5 MeV/u collisions of highly stripped ions with inert gas atoms. From these calculations, he also derived (Schlachter et al., 1982) an approximately half-Rutherford scattering formula (in which the target atom was assumed to be neutral during the first half of the collision) which was used to predict recoil-ion energies,

$$E_R \text{ (in eV)} = (4\times10^{-4})p^2q^2/(M_tE_pb^2) \qquad (2.2)$$

with M_t the target mass in u, E_p the projectile energy in MeV/u, p and q the respective projectile and target charge states in units of e, and b the impact parameter units of a_o. Cocke (1979) found that Olson's cross-section results agreed well with his experimental data for single ionization but predicted too much multiple ionization, while calculations based on the ED model accounted for many features of the higher-charge-state data. More recent CTMC calculations including a quantum-statistical semiclassical description of the time evolution of electron densities in rare gas atoms have been presented by Horbatsch (1986), and agree substantially better with experimental results for both low and high states of ionization.

Low-energy collision experiments have been performed with recoil ions inside various ion traps (Vane et al., 1981; Prior et al., 1983; Church et al., 1983; Church et al., 1985) in order to determine charge-transfer rates of multiply-charged neon ions with the neutral background gas at low energies. Estimates of stored ion mean energy ($\lesssim$1-2 q eV, for q = 2,3,4) inside the Penning ion trap were made by examining the ion number stored as a function of trapping potential well depth (Holmes et al., 1982).

Interest in multiple electron-capture phenomena at low velocities has prompted the use of secondary beams of highly-charged recoil ions in collisional studies in the 0.1-to-few keV-per-charge energy range. Cocke et al. (1981) and Justiniano et al. (1981) studied collisions of slow argon ions with inert gases by determining the initial and final charge states of the projectile ions, as well as the final charge states of the target ions. Total cross sections for low-energy inert-gas ions impinging on helium were later measured (Justiniano et al., 1984) in the same manner.

Liljeby et al. (1986) improved the efficiency of such measurements by determining all charge-state parameters purely by time-of-flight techniques, thus collecting all ions rather than selecting particular reaction channels. They presented a comprehensive set of absolute cross section data for collisions of 1.8 q keV argon ions with neon, argon and krypton, and derived a model (Bárány et al., 1985; Hvelplund et al., 1985) to explain their data. Upper limits on argon recoil-ion energies (>0.25 eV for Ar^{+}, 1 eV for Ar^{2+}, etc., up to 25 eV for Ar^{9+}) were determined from the widths of the time-of-flight peaks (Liljeby et

al., 1986). A lower emmitance source of highly-charged ions is needed, however, to extend the velocity regime of such experiments below 100 eV, since beam divergence and energy spreads arising from recoil-ion energies become appreciable in this energy range.

Despite the abundance of research concerning recoil ions, it is surprising to note that very little information (other than upper limits) exists regarding the energy and angular distributions of the primary recoil ions themselves. Although Beyer et al. (1982) obtained an energy distribution for argon recoil ions by deconvoluting the Doppler broadening of Auger electron lines, and González Lepera et al. (1987) investigated angular distributions of neon recoil ions, virtually no other data of these types existed prior to the present work. However, very recent cross section and recoil energy measurements for ions created in extremely-fast collisions of highly-charged uranium ions with inert-gas targets have been made (Ullrich et al. 1987), which complement the results herein.

CHAPTER 3

EXPERIMENTAL METHOD

Time-of-Flight Technique

The time-of-flight (TOF) technique is a very efficient method of identifying the charge-to-mass ratio of ions created under experimental conditions. TOF analyzers permit, in principle, collection of all ions produced, in contrast to conventional electrostatic and magnetic analyzers which select only a narrow passband and must be scanned over the range of interest.

The simplest TOF spectrometer consists of a source region, where the ions are created in the presence of a constant electric field, and a field-free drift region with a particle detector at the end opposite the source (Figure 3.1). The ions are swept from the source region by the electric field and attain a final velocity proportional to $(q/m)^{1/2}$, where q and m are ion charge and mass respectively (Appendix A). They are allowed to drift at this velocity in the field-free region and are then detected. If the time of flight from the instant of creation to the instant of detection is measured, the charge-to-mass ratio of each particle may be determined.

Poor resolution in TOF spectrometers may arise from several different sources. The flight time of a particular ion must be measured accurately to distinguish it from ions of different (q/m). This measurement becomes increasingly difficult for short flight times. Typical experimental flight times are often on the order of a microsecond (μs) or less, requiring apparatus with a timing resolution

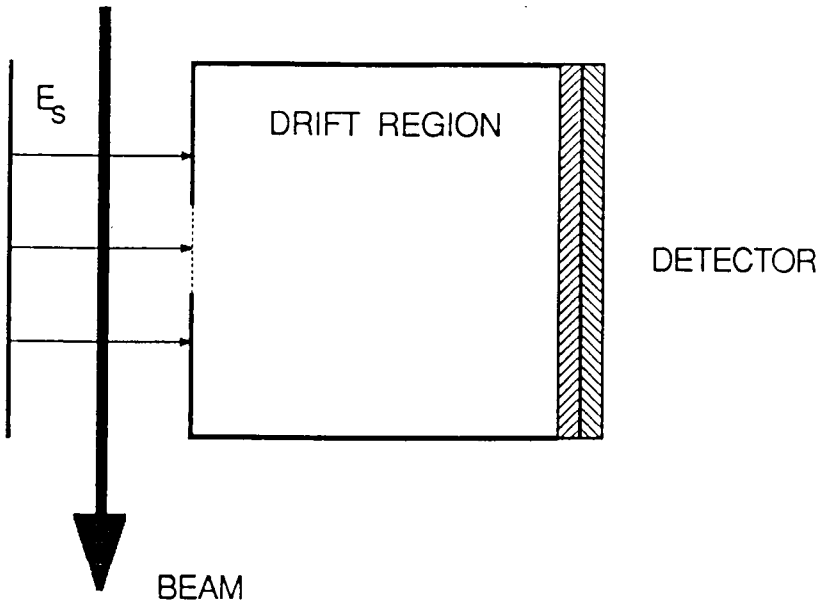


Figure 3.1. Schematic of a two-stage TOF spectrometer. Ions are extracted from the source region by the electric field E_S and allowed to drift in the field-free region. Ion (m/q) is determined from measured flight time.

of nanoseconds (ns) or less. Standard fast timing electronics, used with the proper particle detectors and time pick-off techniques, can provide suitable timing properties on the nanosecond scale. Nonetheless, a finite uncertainty due to electronic walk, drift, and jitter is unavoidable. Walk is the uncertainty in time measured between two pulses due to variations in the shape and amplitude of pulses; drift is the timing error introduced by component aging and temperature variations; and jitter is the time uncertainty caused by noise and statistical fluctuations of the signals from the detectors (Paulus, 1985).

Other contributions to poor timing resolution would arise even if absolute timing accuracy were possible. Ions created at different positions within the source region may have varying path lengths to the detector, resulting in a spread of flight times for ions with the same charge and mass. Also, ions traversing different paths may experience slightly different electric fields due to field fringing and other imperfections in the surfaces of the spectrometer. Another source of variation in actual flight times arises from the kinetic energy the ions have at the moment of creation. All ions have thermal energy and may acquire some recoil energy (E_R) during creation. The largest difference in flight times for two identical ions, each with initial energy (U_o), occurs if one ion is originally headed directly towards the detector and the other directly away from the detector. The ion originally traveling away from the detector will be turned around by the electric field in the source region and return to its original position acquiring the same U_o, but with a velocity opposite to its initial one. The difference in flight times for these two ions is the time it takes the ion headed away from the detector to turn around and return to its initial position. A distribution of initial kinetic energies, or velocities, will consequently result in a spread of flight times for each ion species.

Field fringing may be minimized in the design of TOF spectrometer components by using clean, flat, smooth surfaces and by placing high-transmission, fine grids at all apertures. By proper selection of spectrometer dimensions and field strengths, it is possible to eliminate (to first order) variations in flight times arising from the

finite source width (Wiley and McLaren, 1955). Ions created at different locations within the source electric field have different final velocities when they enter the drift region, because they are accelerated over different distances; the ones created farther from the detector can thus be made to arrive at the detector with the same flight time, an effect known as space focusing (Wiley and McLaren, 1955). Wiley and McLaren found that by introducing an additional acceleration region immediately after the source field region (Figure 3.2), one could space focus quite accurately.

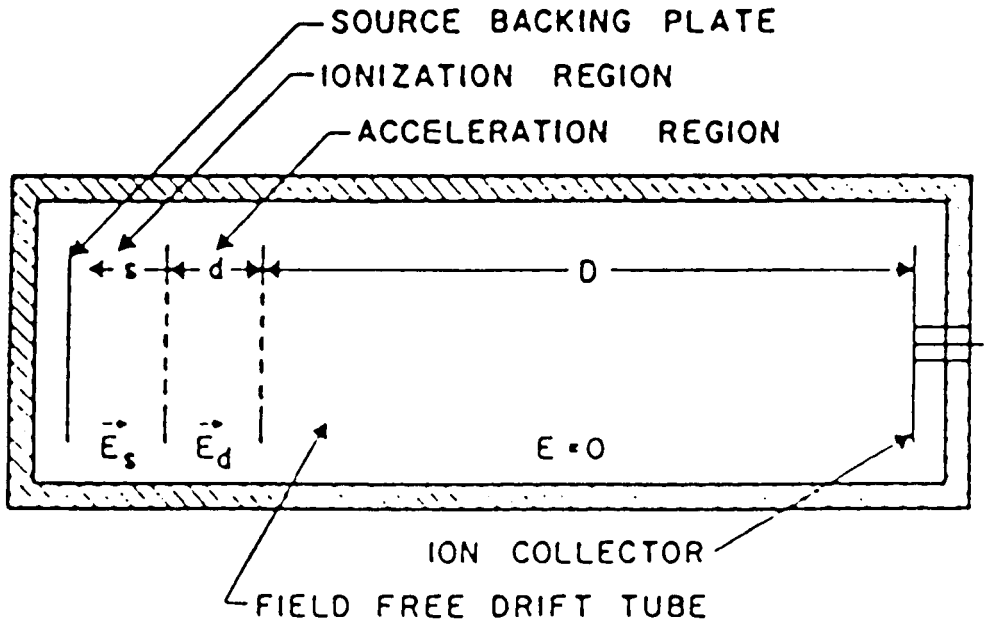


Figure 3.2. TOF spectrometer of Wiley and McLaren design. Space focusing is provided by the addition of a second electric field region (E_d) and by proper choice of E_s/E_d.

Source: Wiley, W. C., and I. H. McLaren, 1955, Rev. Sci. Instrum. **26**, 1150.

The spread in flight times resulting from a distribution of initial kinetic energies or velocities, however, cannot be eliminated (Wiley and McLaren 1955) if a DC electric field is used in the source region. It can only be reduced fractionally by making the initial energy a smaller fraction of the final total energy the ions acquire in the spectrometer (i.e., by accelerating the ions with stronger electric fields). Useful information may be gained, however, by exploiting this feature of TOF spectrometers in order to investigate the recoil energy that ions gain during formation.

Time-of Flight Spectrometer

The TOF spectrometer used in the experiments described below was designed by Liljeby and Danared (1984), with slight modifications for the present use. This design differs from that of Wiley and McLaren (1955) in that an additional field region and drift region have been added. These additions provide space focusing, but in a much shorter overall distance (<25%) than the more common Wiley and McLaren type TOF spectrometer. Short length is important to keep flight times of interest in the range between successive bursts of synchrotron radiation, and event statistics benefit from a short timing cycle, since more cycles are accommodated in the beam time available. Ion collection efficiency should also be higher for a shorter spectrometer.

Figure 3.3 is a schematic of the TOF spectrometer used. The source region is a gas cell, maintained typically at a pressure of $\lesssim 1$ mTorr. Since good vacuum outside the gas cell is necessary to minimize collisions of ions with background gas while they traverse the spectrometer, all components of the spectrometer were constructed of

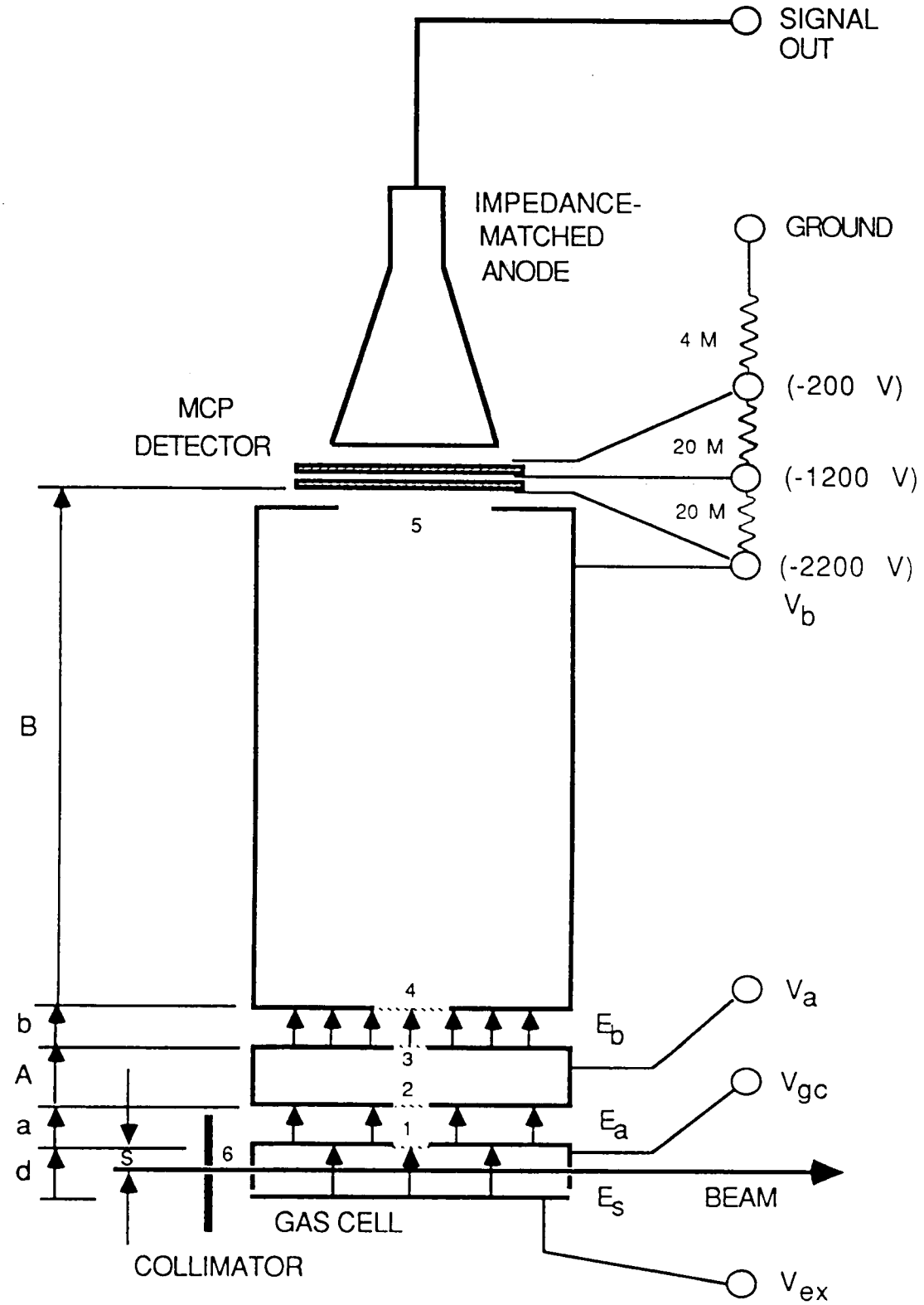


Figure 3.3 TOF spectrometer used in present experiments. Table 3.1 contains critical dimensions of spectrometer.

materials compatible with ultra-high vacuum ($\lesssim 10^{-7}$ Torr). The conducting parts are either locally machined stainless steel (SS) pieces, or SS "eV Parts" available from Kimball Physics Company (1982). Insulating components are constructed of alumina rods and spacers (Kimball Physics, Co. 1982), MACOR, and Teflon sheet. All apertures are circular and are covered by a fine (88% transmission) SS mesh to reduce lens focusing effects. Critical dimensions of each section are listed in Table 3.1. The overall distance from the center of the incident beam to the detector face is about 9.5 cm. The spectrometer is mounted on a stainless steel plate which contains two gas lines, each constructed of 1/4 inch SS tubing. One is a gas inlet line, and the other is for measurement of pressure inside the gas cell (source region).

Table 3.1. Critical dimensions of TOF spectrometer. Figure 3.3 is a schematic of spectrometer.

Nomenclature		Length (cm)	Aperture	Diameter (cm)
Beam center to first aperture	(s_o)	0.30	Gas cell exit (1)	0.32
Acceleration	(a)	0.51	Region a exit (2)	0.48
Drift	(A)	0.76	Region A exit (3)	0.48
Acceleration	(b)	0.38	Region b exit (4)	0.64
Drift	(B)	7.6	Region B exit (5)	2.22
Source width	(d)	0.75	Incident beam (6)	0.20

Voltages are applied to electrodes (Figure 3.3) in the spectrometer creating electric fields in three regions, designated by E_s, E_a, and E_b. The detector is a Galileo Electro-Optics model FTD-2003 dual chevroned microchannel plate (MCP) assembly with a 50 ohm impedance-matched anode (Wiza, 1979; Galileo Electro-Optics Corp., 1980). Impedance matching minimizes reflections of detector signals, thereby enhancing electronic timing resolution. A voltage divider external to the vacuum system is used to maintain the appropriate voltages at the MCP assembly entrance, center, and exit. The anode is maintained at ground potential. Detector strip current (typically ~55 μA) is measured in parallel with current through the voltage divider to monitor detector stability.

The ion energy U (in eV) after acceleration by the series of electric fields E_s, E_a, and E_b (in V/cm) is

$$U = U_o + qsE_s + qaE_a + qbE_b \qquad (3.1)$$

where U_o is ion initial energy (in eV), q is the charge of the ion (in e), and s, a, and b are the distances (in cm) through which the ion is accelerated by each respective field. Flight times (in μs) in each region of the TOF spectrometer (Figure 3.3) for an ion with mass m (in u) and charge q (in e), created a distance s (in cm) from the first aperture, are given in Equations 3.2 - 3.6. The factor (1.02) in each equation arises when $(m/q)^{1/2}$ is converted to the above units from MKS units by evaluating $(u/e)^{1/2}$ (Appendix A).

$$T_S = (1.02)\frac{(2m)^{1/2}}{qE_S}\left[(U_S)^{1/2} \mp (U_O)^{1/2}\right] \qquad (3.2)$$

$$T_a = (1.02)\frac{(2m)^{1/2}}{qE_a}\left[(U_a)^{1/2} - (U_S)^{1/2}\right] \qquad (3.3)$$

$$T_A = (1.02)\frac{A(2m)^{1/2}}{2(U_a)^{1/2}} \qquad (3.4)$$

$$T_b = (1.02)\frac{(2m)^{1/2}}{qE_b}\left[(U)^{1/2} - (U_a)^{1/2}\right] \qquad (3.5)$$

$$T_B = (1.02)\frac{B(2m)^{1/2}}{2(U)^{1/2}} \qquad (3.6)$$

The energies U_S and U_a (in eV) characterize the ion after each respective acceleration region; A and B are the lengths (in cm) of the subsequent drift regions. The minus sign in Equation 3.2 is used for ions originally headed directly toward the detector, and the plus sign for ions originally headed directly away. The total flight time (T) is the sum of the above equations

$$T = T_S + T_a + T_A + T_b + T_B. \qquad (3.7)$$

If U_o is assumed to be negligible ($\cong 0$), and each electric field is expressed in terms of the product of a scaling parameter κ and a

nominal field value ε_i (e.g., $E_S = \kappa\varepsilon_S$) the equations simplify, exhibiting an $(m/q\kappa)^{1/2}$ dependence of total flight time

$$T(U_o=0) = (1.02)\frac{(2m)^{1/2}}{(q\kappa)^{1/2}}\left[\frac{(s)^{1/2}}{(\varepsilon_S)^{1/2}} + \frac{(s\varepsilon_S - a\varepsilon_a)^{1/2}}{\varepsilon_a} + \frac{A}{2(s\varepsilon_S + a\varepsilon_a)^{1/2}} + \frac{(b\varepsilon_b - a\varepsilon_a)^{1/2}}{\varepsilon_b} + \frac{B}{2(s\varepsilon_S + a\varepsilon_a + b\varepsilon_b)^{1/2}}\right]. \quad (3.8)$$

The maximum time spread about $T(U_o=0)$ introduced by a non-zero U_o is the time (ΔT_u) it takes an ion originally directed away from the detector to turn around and return to its original position (Appendix A),

$$\Delta T_u = (1.02)\frac{2(2mU_o)^{1/2}}{qE_S}. \quad (3.9)$$

Calculated flight times for argon charge-state-four ions created at different locations (s) within the source region, and with different initial energies are listed in Table 3.2. The electric field values were selected for optimum space focusing, which is demonstrated by the similarities in flight times for different values of s; the effect of U_o on flight time is also evident.

The three major sources of spread in ion flight times depend differently on TOF spectrometer field values (and therefore on κ).

Table 3.2. Calculated flight times for Ar^{4+} ions in TOF spectrometer using nominal optimum electric field values. Positive (negative) values of U_o indicate ions originally headed directly toward (away from) detector. Electric field values used are (in V/cm): E_s = 597.3 ; E_a = 578.4; and E_b = 5013.

s (cm)	U_o (eV)	T (μs)
0.20	0	0.6282
0.30	0	0.6279
0.40	0	0.6283
0.30	+0.1	0.6267
0.30	-0.1	0.6291
0.30	+1.0	0.6241
0.30	-1.0	0.6317

The inherent electronic timing spread (ΔT_e) is independent of spectrometer parameters or ion properties. The time spread (ΔT_f) due to small variations in each electric field, as well as from variations in initial position (s) within the source, scale with total flight time as $1/(q\kappa)^{1/2}$. However, initial kinetic energy produces a spread (ΔT_u) that scales as $1/(q\kappa)$, as Equation 3.9 shows with $E_s = \kappa\varepsilon_s$. If these independent contributions are added in quadrature (assuming Gaussian distributions) the total time spread measured for a particular ion (m,q) can be expressed as

$$(\Delta T)^2 = (\Delta T_e)^2 + (\Delta T_f)^2 + (\Delta T_u)^2. \qquad (3.10)$$

The space focusing property (minimum $\Delta T_f/T$) which is characteristic for a set of electric fields ε_s, ε_a, and ε_b, is preserved for all sets of fields obtained by multiplication of each by a common scaling parameter κ. Consequently, Equation 3.10 can be rewritten including the $1/q\kappa$ dependence of each term,

$$(\Delta T)^2 = \alpha + \beta(1/q\kappa) + \gamma(1/q\kappa)^2. \qquad (3.11)$$

Here, α, β, and γ are assumed constant for each gas and represent flight time spreads arising from electronic timing fluctuations, field fringing (and variations in s), and ion energy, respectively. An average initial ion energy $\bar{U}_o$ following creation by a particular process (e.g., photoionization or ion impact) can then be determined as follows. Time-of-flight spectra are obtained for several values of κ, and the time spread for each ion species is found by extracting the full-width-at-half-maximum (FWHM) of each (m/q) peak in each TOF spectrum. These spreads (ΔT) are fitted to Equation 3.11, from which the constants α, β, and γ are found. The value of $\bar{U}_o$ is calculated from the parameter γ using Equations 3.9, 3.10, and 3.11,

$$\bar{U}_o = \frac{\gamma(\varepsilon_s)^2}{(1.02)^2(8m)} \quad . \qquad (3.12)$$

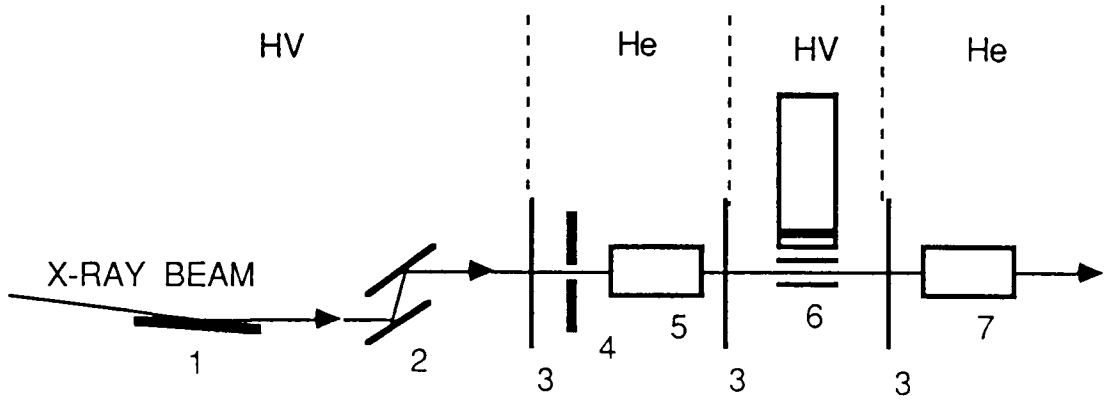
The value of $\bar{U}_o$ is a weighted average of the distribution of U_o. It is considered to be a representative value of U_o, but is not necessarily the mean energy in the strictest sense. Motion parallel to the TOF

spectrometer axis is measured by this technique. There is no direct contribution to the flight time from velocity components perpendicular to this axis.

Stanford Synchrotron Radiation Laboratory Setup

The TOF spectrometer was mounted vertically from the top flange of an ultra-high-vacuum (UHV) chamber at the end of experimental beamline IV-2 on the electron-positron storage ring (SPEAR) at Stanford Synchrotron Radiation Laboratory (SSRL). The experiment chamber was secured on top of an adjustable table inside a protective hutch. Base vacuum of $\sim 5\times10^{-7}$ Torr, as measured by a Varian model 580 nude ionization gauge and model 880 controller, was maintained by a Balzers model 510 turbomolecular pump (pumping speed of ~500 l/sec); chamber vacuum was isolated from the SPEAR vacuum system by berylium windows. A helium atmosphere was necessary between the end of the SSRL beamline and the experiment chamber to minimize absorption of synchrotron radiation, and was maintained by enclosing the open area with plastic sheets and allowing helium to flow slowly through the enclosed region.

Intense beams of white (and later monochromatic) x rays from an eight-pole wiggler operated at 15 kGauss were focused by a platinum-coated toroidal quartz-crystal mirror, and then collimated using a four-jaw slit assembly placed in the helium atmosphere between the beamline and chamber berylium windows (Figure 3.4). Beam spot size at the position of the gas target was less than 2 mm x 2 mm. Beam transmission through the experimental apparatus was optimized by adjusting the experiment table height and tilt, as well as the



HV - High Vacuum
He - Helium Atmosphere

1. Mirror
2. Monochromator (when inserted)
3. Beryllium Window
4. Four-jaw Slits
5. Helium Ionization Chamber
6. TOF Spectrometer
7. Argon Ionization Chamber

Figure 3.4. Schematic of the SSRL beamline and TOF experiment chamber.

horizontal angle between the chamber and beamline axis, using stepping motors driven by controllers external to the hutch.

The critical energy (equal power is radiated above and below the critical energy) of the radiation was 4 keV, corresponding to the 2-GeV electron beam in the storage ring and 15 kGauss wiggler field. The spectral distribution was severely attenuated below 3 keV by the berylium windows (total combined thickness of 25 mil) and above 10 keV by the focusing mirror. Figure 3.5 shows typical spectral distributions of radiation from a six-pole wiggler when operated at 18 kGauss (fewer poles than used in present experiment, but operated at a higher field, thus serving as an approximate comparison). Photon

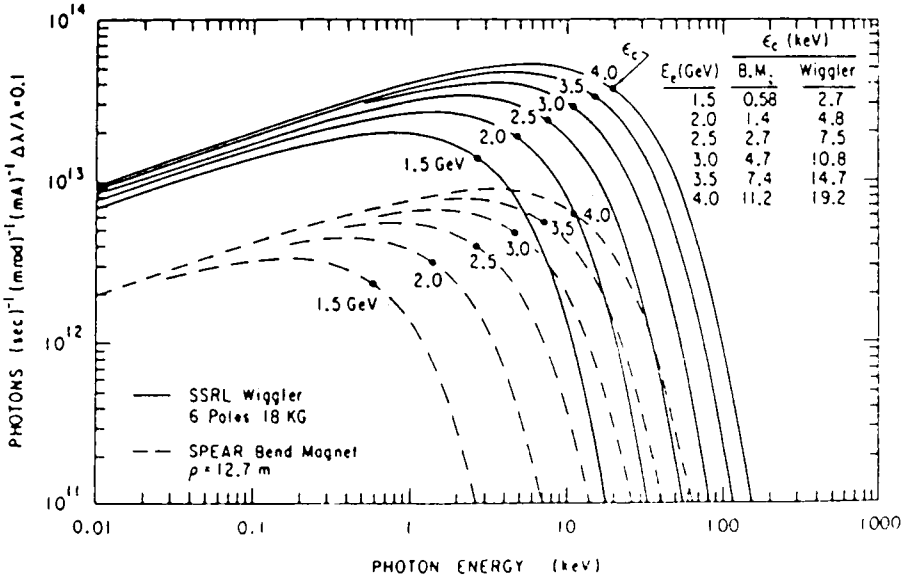


Figure 3.5. SPEAR bending magnet and SSRL wiggler spectra for various stored electron energies, E_e.

Source: Bienenstock, A., 1980, Nucl. Instrum. Meth. 172, 13.

(x-ray) flux was measured using helium and argon ionization chambers, upstream and downstream of the target chamber, respectively.

SPEAR was operated in single-bunch mode (colliding beam experiments were simultaneously in progress) with typical stored electron beam currents of ~10 mA. The electron-bunch orbital frequency was 1.28 MHz, producing x-ray bunches of approximately 300 ps width (White et al 1979), at evenly spaced intervals of 781 ns. The (1.28 MHz) RF signal used to maintain stored beam energy was available as an excellent timing reference to determine the instant of ion creation inside the target gas cell. Although the RF pulse did not necessarily coincide with the moment of ion creation, there was a very stable constant phase between the two events.

Target gas was leaked slowly through a needle valve into the production gas cell, producing a target pressure of ~0.5 mTorr, as measured by an MKS model 370HA-0001 Baratron (capacitance manometer). The background chamber pressure rose to ~1.5×10^{-6} Torr at this gas cell pressure. Neon, argon, krypton, and xenon ions were produced by inner-shell photoionization of the neutral target gases. Ions created inside the gas cell were extracted through the 3 mm diameter aperture into the TOF spectrometer, and were subsequently detected by the Galileo Electro-Optics Model FTD-2003 dual chevroned microchannel plate (MCP) assembly and 50 ohm impedance matched collector anode (Wiza, 1979; Galileo Electro-Optics Corp., 1980).

TOF spectrometer extraction plate, gas cell and drift region A voltages were supplied by Tennelec model TC952 3 kV power supplies. A digital display of each applied voltage facilitated accurate

reproducibility of field values, as E_s, E_a, and E_b were varied to determine $\bar{U}_o$ for each ion species. Drift region B and the MCP detector entrance were held at -2.2 kV by a Tennelec model TC950 5 kV bias supply.

Figure 3.6 illustrates the timing scheme used to accurately measure the flight time of each ion detected. Excellent resolution is critical to the determination of $\bar{U}_o$, otherwise the TOF peaks for different mass isotopes would be hopelessly smeared, making measurements of peak widths (ΔT) impossible for neon, krypton and xenon. Fast timing requires careful impedance matching of all components and cables in order to minimize reflections of signals. All components were connected with 50 ohm RG-58/u coaxial cable and BNC connectors, or with RG-174/u cable and LIMO connectors where appropriate. The negative fast-rise-time ion-detector pulses were amplified by an Ortec model 9301 fast preamplifier followed by two stages (each x10 amplification) of an Ortec model 574 timing amplifier (TA). The amplified detector output and storage ring RF reference signals were each fed to Tennelec model TC454 quad constant fraction discriminator (CFD) stages, which were tuned to reduce electronic time walk due to variations in pulse shape and height. The output of the storage-ring RF CFD stage was connected to the start input of a LeCroy model 4201 CAMAC time-to-digital converter (TDC); the output of the ion detector CFD stage was connected to the stop input. Ion count rates from the CFD were monitored using a Tennelec model TC536 counter/timer. The digital output of the TDC (corresponding to tne time elapsed between the start input and the stop input) was

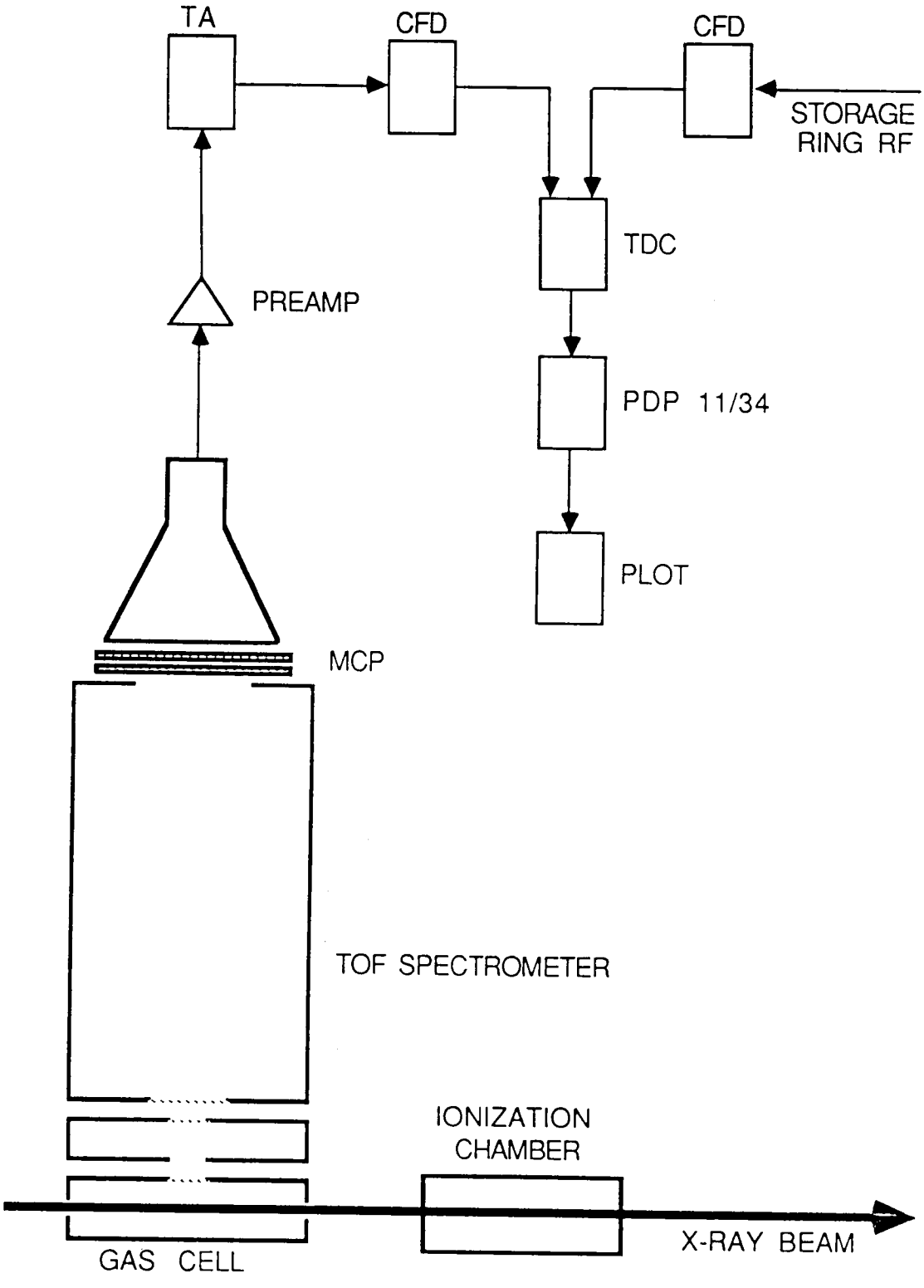


Figure 3.6. Schematic of ion TOF apparatus at SSRL. The storage ring RF is used as a timing reference to measure ion flight time.

transferred via standard CAMAC interfaces to a PDP-11/34 computer available at the beamline.

The TOF spectra were accumulated and stored as multi-channel arrays consisting of 6000 channels, each 0.156 nanoseconds wide, covering a total time of 937.5 nanoseconds. Each channel corresponded to a small range of flight times, and the number of ions with flight times in each range was stored in the appropriate channel. The TOF spectra could be displayed on a Tektronix 4010 graphics terminal by an interactive FORTRAN program.

Photon flux through the target cell was estimated to be $\sim 10^{+13}$ photons mm^{-2} sec^{-1} from ionization chamber current and known photo-absorption cross sections (McMaster, 1969) when using white light. Typical total ion count rates ranged from ~200 Hz (neon) to ~5 kHz (xenon) and depended on target gas used, since photoionization cross sections scale as Z^5 (Heitler, 1936). For each target gas, a series of TOF spectra was taken at four different sets (κ = 1, 1/2, 1/4, 1/8) of proportionately scaled spectrometer fields. Values of electrode voltages, and corresponding field values, for each set are listed in Table 3.3. To optimize the space focusing condition, the calculated optimum values for each electric field in the spectrometer were initially used, and then the voltage applied to the extraction plate (V_{ex}) was adjusted to obtain the most symmetric peak shapes with minimum width at the lowest (κ = 1/8) field strength settings (the space focusing condition is most sensitive to the field in the source region). Ion count rates were sufficient to obtain high statistics

spectra (e.g., signal-to-noise ratio of $\geq$500:1) in $\leq$30 minutes at each setting.

From these sets of TOF spectra, average energies ($\bar{U}_o$) and average charge states ($\bar{q}$) were determined (Chapter 4) for ions produced by inner-shell photoionization of neon, argon, krypton, and xenon . In order to assure uniform detection efficiency for each charge state, only spectra obtained using maximum field strengths (κ = 1) were used for $\bar{q}$ measurements. At these voltages all ions of interest arrived at the detector with $\geq$8 keV energy, providing approximately uniform detection efficiency for all charge states (Burrous, 1967).

A Si(111) double-crystal monochromator (Figure 3.4), with band pass of 1 × 10^{-4}, was inserted and used to tune the radiation above, below, and interleaving the L_1, L_2, and L_3 edges of xenon to explore the effects on final charge-state distributions. Xenon TOF spectra were obtained using photon energies of 4750 eV, 5050 eV, 5400 eV, and

Table 3.3 TOF spectrometer operating parameters at SSRL. Figure 3.3 is a schematic of the spectrometer.

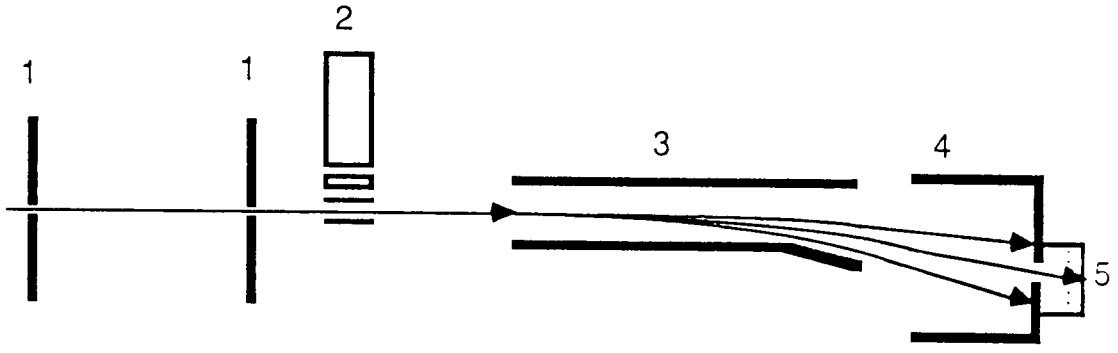
κ	V_{ex} (V)	V_{gc} (V)	V_a (V)	V_b(V)	E_s (V/cm)	E_a (V/cm)	E_b (V/cm)
1	3640	2200	1610	-2200	1920	1157	10,030
1/2	720	0	-295	-2200	960	578	5013
1/4	-740	-1100	-1248	-2200	480	290	2505
1/8	-1470	-1650	-1724	-2200	240	145	1253

5475 eV. Although the photon flux was severely reduced ($\geq$2 orders of magnitude) by use of the monochromator, each spectrum was obtained within several hours. Maximum spectrometer electric field strengths were again used in order to assure uniform detection efficiency.

Oak Ridge National Laboratory Setup

The TOF spectrometer was mounted horizontally on an adjustable platform inside a stainless steel scattering chamber on the 135 degree beamline of the EN Tandem Van deGraaff Accelerator in Building 5500 at Oak Ridge National Laboratory (ORNL). The experiment chamber was connected to the accelerator vacuum system, and base vacuum of $\sim 5 \times 10^{-7}$ Torr, as measured by a Varian model 580 nude ionization gauge and model 880 controller, was maintained by Varian model 0183 and 0184 diffusion pumps. Accelerator beams of ~0.5 - 1 MeV/u chlorine ions were magnetically charge-state and momentum selected and then collimated by two four-jaw slit assemblies, about 2 meters apart, located upstream of the target chamber (Figure 3.7). Beam spot size at the position of the gas target was less than 1mm x 1mm. The collimators and spectrometer had been optically aligned along the nominal beam path prior to obtaining vacuum. Beam current was measured by a Faraday Cup (FC) located downstream of the TOF spectrometer, and was optimized with electrostatic and quadrupole focusing lenses on the accelerator beamline.

It was also possible to charge-state analyze the post-collision projectile beam using electrostatic deflection plates (Figure 3.7). Selected charge states could be deflected through a slit in the FC, and individual scattered beam ions of a particular charge state could be



1. Four-Jaw Slits
2. TOF Spectrometer
3. Electrostatic Deflection Plates
4. Faraday Cup
5. Parallel Plate Avalanche Detector

Figure 3.7. Schematic of ORNL beamline and recoil-ion TOF experiment chamber.

counted by a one-dimensional position-sensitive Parallel Plate Avalanche Detector (PPAD) from The University of Frankfurt. Appendix B contains a description of the PPAD and projectile-charge-state analysis system.

The TOF spectrometer was modified from the configuration used at SSRL, to allow detection of electrons ejected during ion formation, by replacing the solid extraction plate with a plate containing a 3 mm diameter aperture (Figure 3.8). A Hamamatsu model F1551-33 three-stage MCP assembly (Hamamatsu, 1983) and collector anode detected electrons which were extracted in a direction opposite to that of the ions by the source electric field.

Target gas was leaked slowly through a needle valve into the production gas cell, producing a typical target pressure of ~0.7 mTorr, as measured by a MKS Model 370HA-0001 Baratron (capacitance manometer). The background chamber pressure rose to $\sim 2\times10^{-6}$ Torr at this gas cell pressure. Recoil ions were produced in single collisions of the projectile ions with the neutral neon and argon atoms. Ions created inside the gas cell were extracted through a 3 mm diameter aperture into the TOF spectrometer, and were subsequently detected by the Galileo Electro-Optics Model FTD-2003 MCP and anode assembly.

Electric fields were established inside the TOF spectrometer in the same manner as at SSRL (previous section). Voltages were applied to the Hamamatsu MCP detector entrance, exit, and anode by Tennelec model TC950 5 kV bias supplies. The anode for the Hamamatsu MCP was held at a high positive potential; therefore, detector signals were

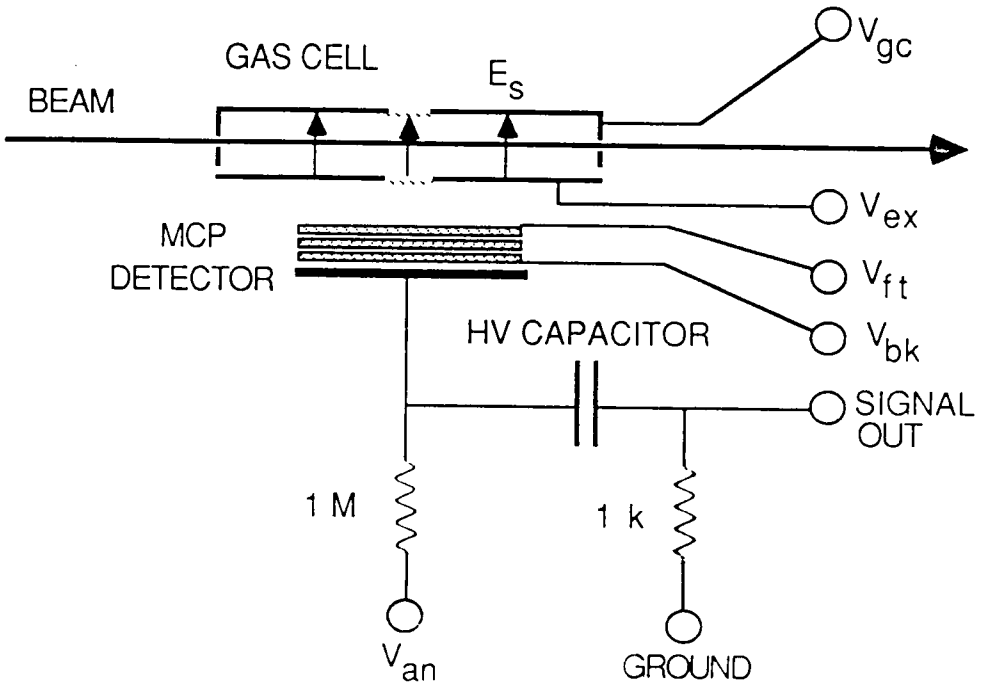


Figure 3.8. Electron detection schematic. Electrons are extracted from the gas cell and detected by an MCP detector.

decoupled from the high voltage by a high-voltage blocking capacitor (Figure 3.8).

Since the ion beams provided by the Tandem accelerator were DC beams (i.e., not pulsed) a timing reference was needed to signify the creation of an ion. Recoil-ion TOF spectra were thus obtained in two different ways. In the first method, recoil ions were detected in coincidence with electrons ejected during ionization and subsequently extracted from the gas cell. The resulting TOF spectra represented ions created in processes where one or more electrons remained in the continuum of the ionized target atom, thus representing essentially a global average of ions created at all impact parameters. In the second method, recoil ions were detected in coincidence with selected

exiting charge states (r = p+1, p+2, p+3, and p+4) of the incident Cl^{p+} projectile beam. In this manner, differential information regarding the correlation between recoil ion production and projectile stripping was gained. Ions produced in coincidence with electron capture (EC), however, were not detected using either method.

In order to estimate the accuracy of each timing reference, as well as to investigate the stability of the electron timing reference as the extraction field was varied, electron-projectile (r = p+1) coincidence spectra were obtained at each TOF spectrometer electric field setting. There was one primary peak in each spectrum, corresponding to coincident detection of an electron ejected in an ionization event and the projectile ion which caused the ionization. This peak width was narrowest at each spectrometer setting when the Hamamatsu detector entrance was held ~100 V more positive than the potential (estimated from source electric field values) at the center of the incident ion beam inside the gas cell. This voltage difference was thus used when obtaining recoil-ion TOF spectra.

Figures 3.9 and 3.10 illustrate the timing schemes used to accurately measure the flight times of each ion detected using the first and second methods, respectively, described above. All components were connected with 50 ohm RG-58/u coaxial cable and BNC connectors, or with RG-174/u cable and LIMO connectors where appropriate. The negative fast-rise-time ion and electron detector pulses were each amplified by an Ortec model 9301 preamplifier followed by an Ortec model 474 timing filter amplifier (TFA). Output signals

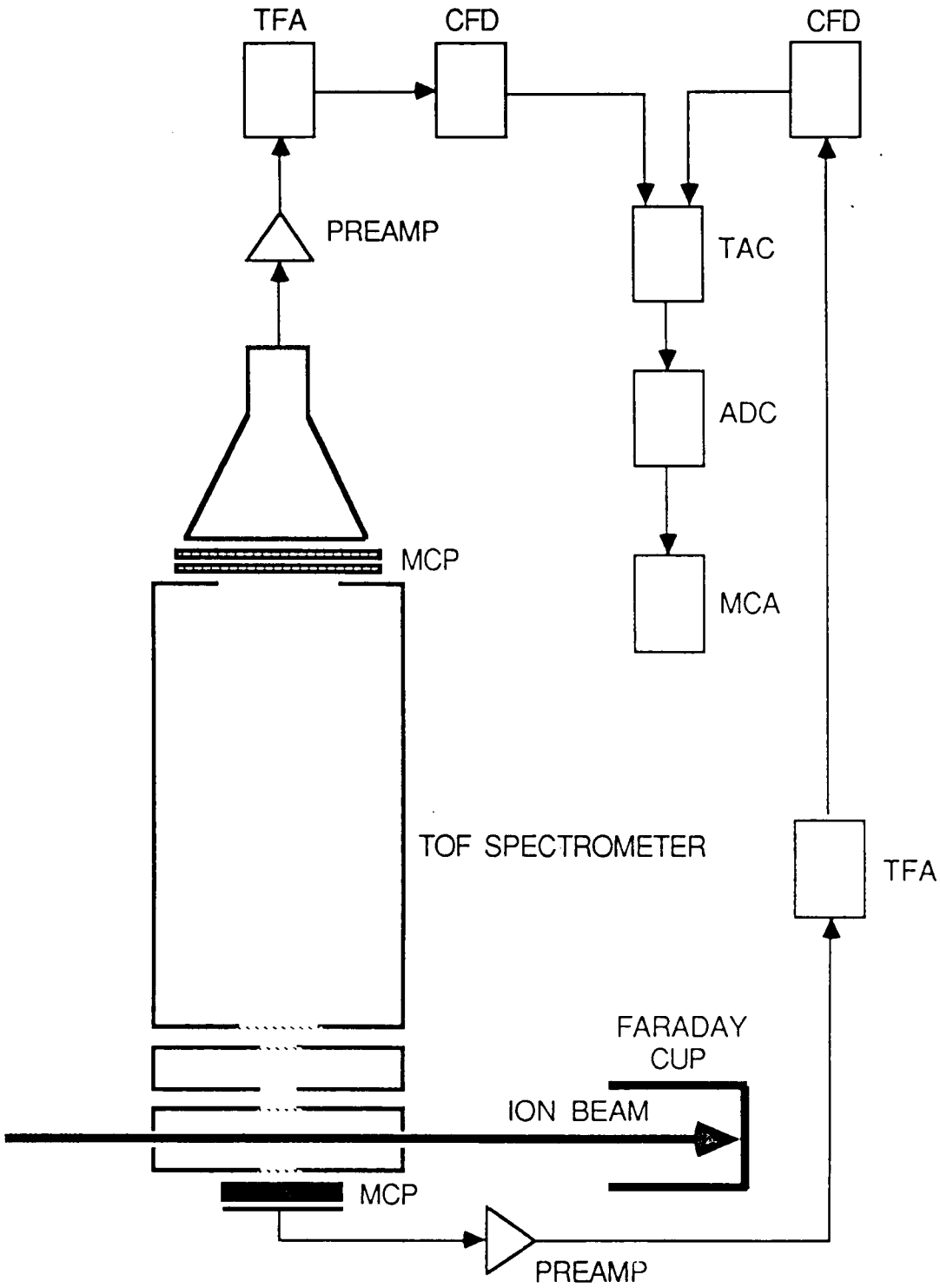


Figure 3.9. Schematic of TOF apparatus for coincident electron and recoil-ion detection at ORNL.

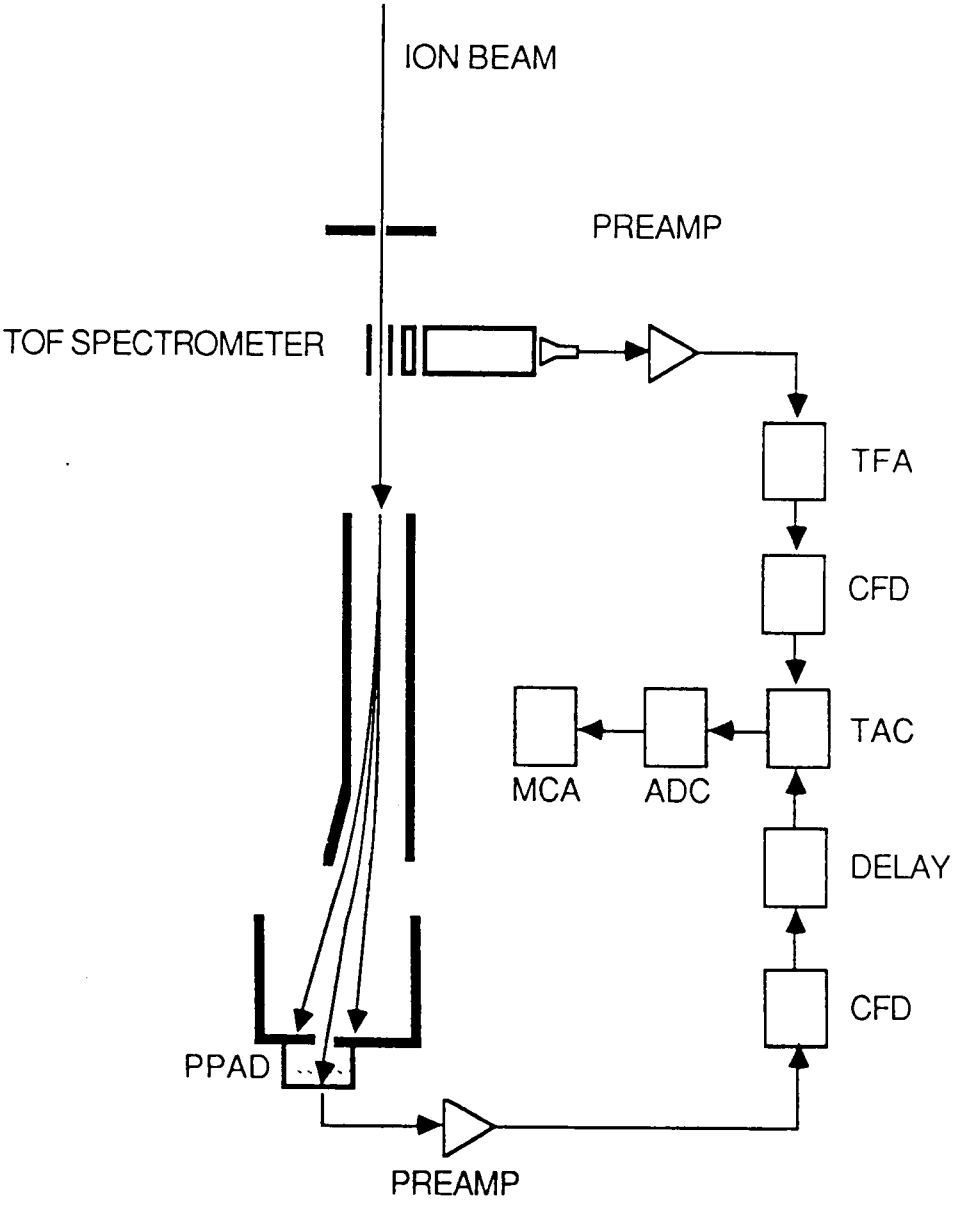


Figure 3.10. Schematic of TOF apparatus for coincident projectile and recoil-ion detection at ORNL.

from the PPAD were amplified by a preamplifier, which was also supplied by the University of Frankfurt (Appendix B). The amplified detector and PPAD output signals were each fed to Tennelec model TC454 quad constant fraction discriminator (CFD) stages, which were tuned to reduce electronic time walk due to variations in pulse shape and height. When using the first timing method, the output of the electron detector CFD stage was the start input of an Ortec model 467 time-to-amplitude converter (TAC), and the output of the recoil ion detector CFD stage was the stop input (Figure 3.9) . When using the second timing method, the CFD output for the recoil ion detector was the TAC start input, and the output of the PPAD CFD stage, delayed by 1.8 microseconds using an Ortec model 416A gate and delay generator, was the TAC stop input (Figure 3.10). In order to obtain electron-projectile coincidence spectra, electron detector CFD output pulses started the TAC and PPAD CFD output pulses stopped the TAC. Ion, electron, and PPAD count rates were monitored at the CFD output stages by Tennelec model TC536 counter/timers.

In all timing modes, the TAC voltage output, which was proportional to the measured ion flight time, was fed to a LeCroy model 3511 analog-to-digital converter (ADC) installed in a LeCroy 3500 Multichannel Analyzer CAMAC crate. The ADC output was accumulated, stored, and displayed as TOF spectra on the LeCroy 3500 (and later saved on diskette). The TOF spectra consisted of 4000 channels, each 0.4 ns wide, covering a total time of 1.6 μs.

Typical beam current through the target cell was ~10 pA. For each target gas and beam energy, a series of TOF spectra was taken at six

different sets (κ = 1, 5/6, 2/3, 1/2, 1/3, and 1/6) of proportionately scaled spectrometer voltages. Electrode voltages, and corresponding field strengths, for each case are listed in Tables 3.4 and 3.5. The optimum calculated spectrometer field values were found to give the most symmetric peak shapes and minimum widths. Typical total ion count rates ranged from 2 kHz to 10 kHz depending on beam current; however, total coincident rates were much lower (~50 Hz to 1 kHz) and depended on the reaction channel selected.

From these sets of TOF spectra, average energies were determined (Chapter 4) for ions created in collisions of 18, 23, 27.6, and 33 MeV Cl^{5+} ions with argon gas, and 22.5 MeV Cl^{4+} ions with neon gas. Both electron and projectile coincidence modes were used for each beam energy, except for 18 MeV Cl^{5+}, for which only the electron coincidence technique was used.

Table 3.4. TOF spectrometer operating parameters at ORNL. Figure 3.3 is a schematic of the spectrometer.

κ	V_{ex} (V)	V_{gc} (V)	V_a (V)	V_b (V)	E_s (V/cm)	E_a (V/cm)	E_b (V/cm)
1	1772	1100	658	-2200	896	867	7521
5/6	1110	550	181	-2200	747	724	6266
2/3	448	0	-295	-2200	597	578	5013
1/2	-214	-550	-771	-2200	448	433	3761
1/3	-876	-1100	-1248	-2200	299	290	2505
1/6	-1538	-1650	-1724	-2200	149	145	1253

Table 3.5. Voltages for electron MCP detector at ORNL. Figure 3.8 is a schematic of the electron detection apparatus.

κ	V_{an} (V)	V_{bk} (V)	V_{ft} (V)
1	3790	3590	1590
5/6	3190	2990	990
2/3	2590	2390	390
1/2	1990	1790	-210
1/3	1400	1200	-800
1/6	800	600	-1400

CHAPTER 4

DATA ANALYSIS

Fitting of Raw Spectra

The time-of-flight (TOF) spectra obtained at SSRL are shown for single inner-shell photoionization of neon (Figure 4.1), argon (Figure 4.2), krypton (Figure 4.3), and xenon (Figure 4.4) using white x rays. Although a continuous spectral distribution of x rays was used (from around 3 to 10 keV), photoionization cross sections (McMaster, 1969) indicate that vacancies were created primarily in the neon K-shell, the argon K-shell, the krypton L-shell, and the xenon L- and M-shells.

Figure 4.5 (parts a, c, and d) illustrates the excellent timing resolution achieved by showing the clear resolution of mass isotopes in the krypton and xenon spectra, in contrast to earlier work (part b) by Hastings and Kostroun (1983). Isotope resolution is necessary for the energy measurements of central concern here; otherwise extraction of an accurate FWHM would be impossible.

Charge states were identified by determining the flight-time differences between adjacent charge states (from the number of channels between centroids of peaks), and then comparing these differences to those of calculated flight times. Since the RF reference signal frequency of 1.28 MHz gave rise to TDC stop pulses every 781 ns, ions with flight times (T) longer than this appear within each spectrum at positions corresponding to flight times (in ns) $T_{eff} = T - 781$ (e.g., xenon charge states two and three in Figure 4.4).

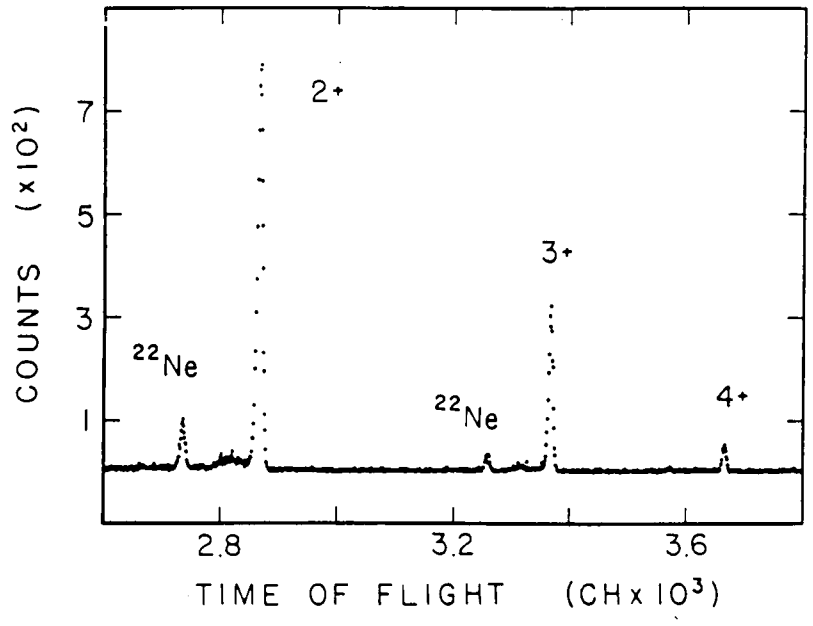


Figure 4.1. Neon TOF spectrum displaying charge-state distribution resulting from production of single K-shell vacancies. Time scale is reversed.

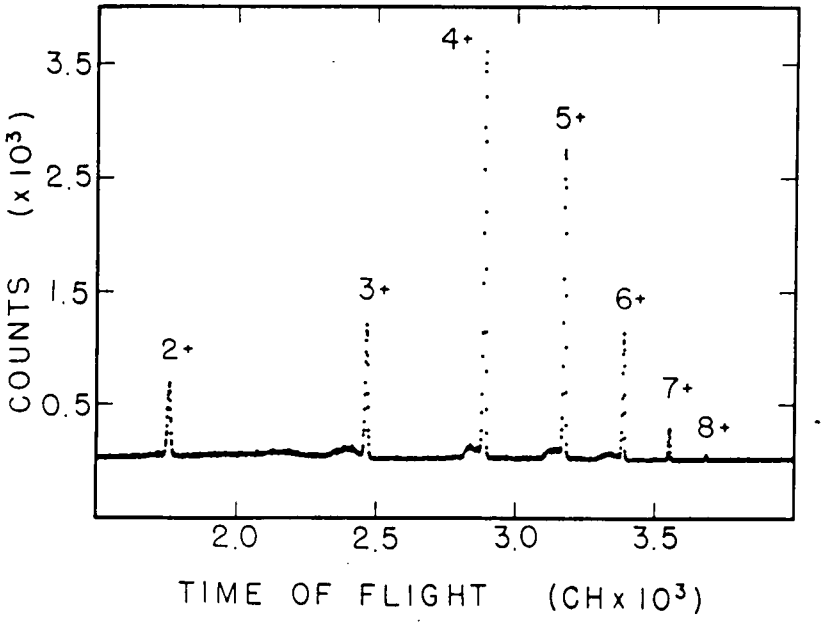


Figure 4.2. Argon TOF spectrum displaying charge-state distribution resulting from production of single K-shell vacancies. Time scale is reversed.

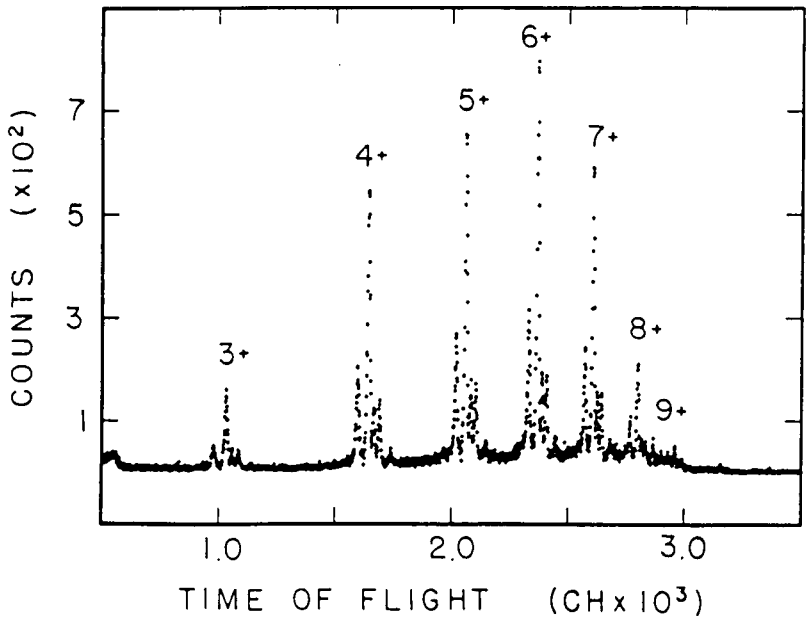


Figure 4.3. Krypton TOF spectrum displaying charge-state distribution resulting from production of single L-shell vacancies. Time scale is reversed.

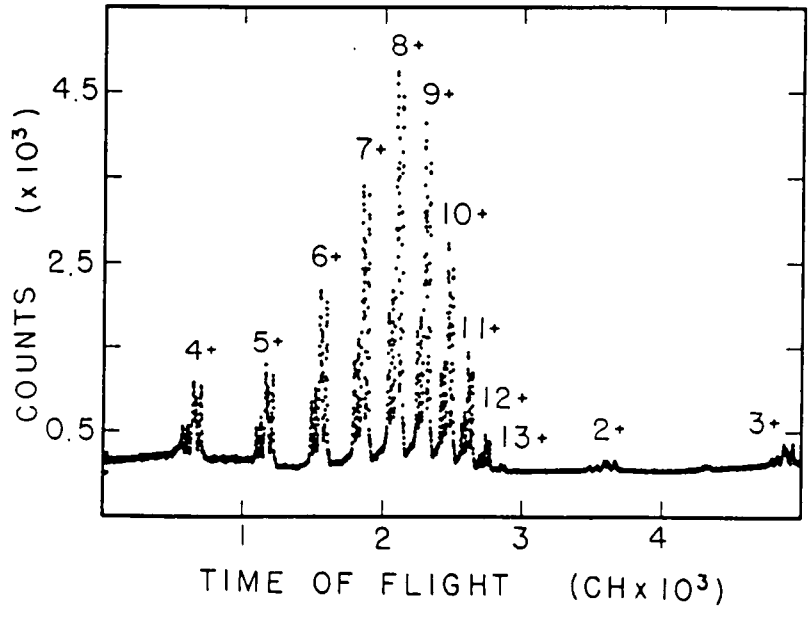


Figure 4.4. Xenon TOF spectrum displaying charge-state distribution resulting from production of single M- and L-shell vacancies. Time scale is reversed.

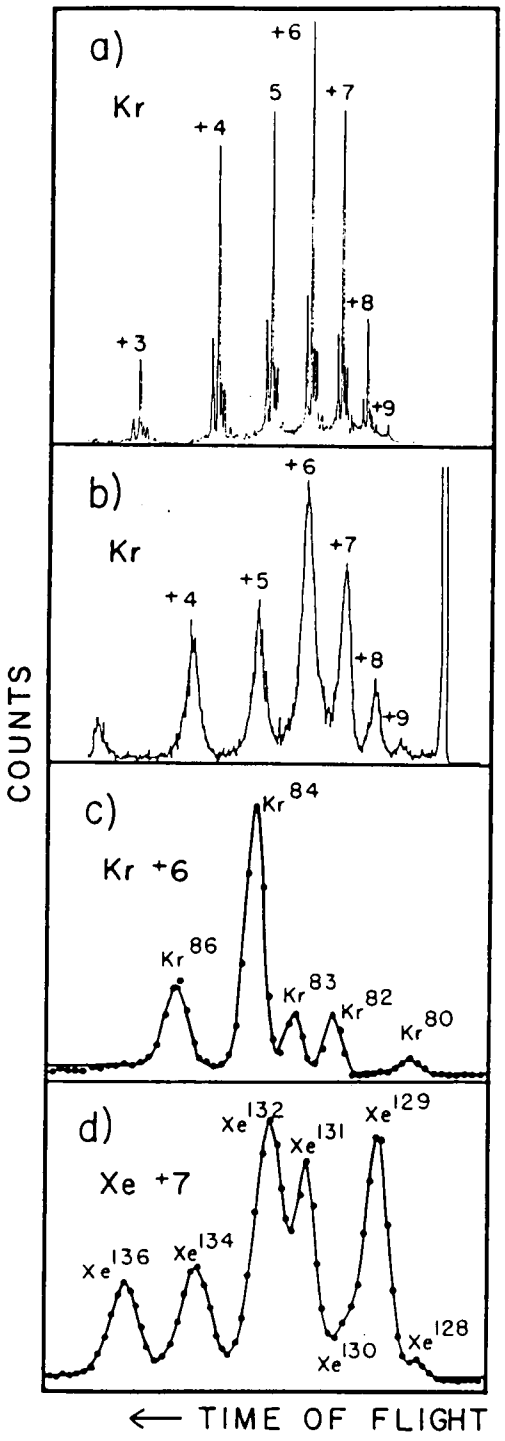


Figure 4.5 Peaks from TOF spectra obtained at SSRL which display mass isotope resolution. (a) Kr charge state distribution following L-shell vacancy production. (b) Earlier work by Hastings and Kostroun (1984) displaying similar results. (c) Expanded view of a Kr peak displaying isotopic resolution. (d) Expanded view of a Xe peak from a typical Xe spectrum.

The TOF data files obtained at SSRL were transferred via hard disk to a VAX 11/780 computer available at SSRL for analysis. An existing FORTRAN program (Levin, 1986) was suitably modified and used to fit the raw data. Each m/q peak of interest was fitted to a Pearson Type VII function (Elderton and Johnson, 1969; Kendall and Stuart, 1943; Kendall, 1948) with a sloping linear background using a non-linear least squares gradient search fitting routine. Pearson Type VII functions are symmetric four parameter functions which can change character continuously from Gaussian to Lorentzian by varying a single parameter. This parameter can be fixed, or allowed to vary from one (Lorentzian) to 100 (Gaussian) during the fitting procedure; for SSRL data, the parameter was fixed to be 100, thus fitting a Gaussian function to each peak. Krypton and xenon spectra, in which adjacent mass isotopes were not fully resolved, were fitted with a superposition of peaks (Figure 4.5). From these fits, the centroid, area, and FWHM of each peak were found, along with the statistical error associated with each parameter.

The area of each peak (background subtracted) corresponded to the number of ions detected (N_q) with a particular m/q. From these areas, the charge-state distributions were determined, and average charge states ($\bar{q} = \Sigma qN_q/\Sigma N_q$) were calculated for those spectra obtained using full electric field strengths ($\kappa = 1$) in the TOF spectrometer.

Figure 4.6 shows how the spread in flight times varied with electric field scaling parameter values (κ = 1, 1/2, 1/4, 1/8). The FWHM increased faster than $(1/\kappa)^{1/2}$, indicating a contribution in spread from the ion kinetic energies (Chapter 3).

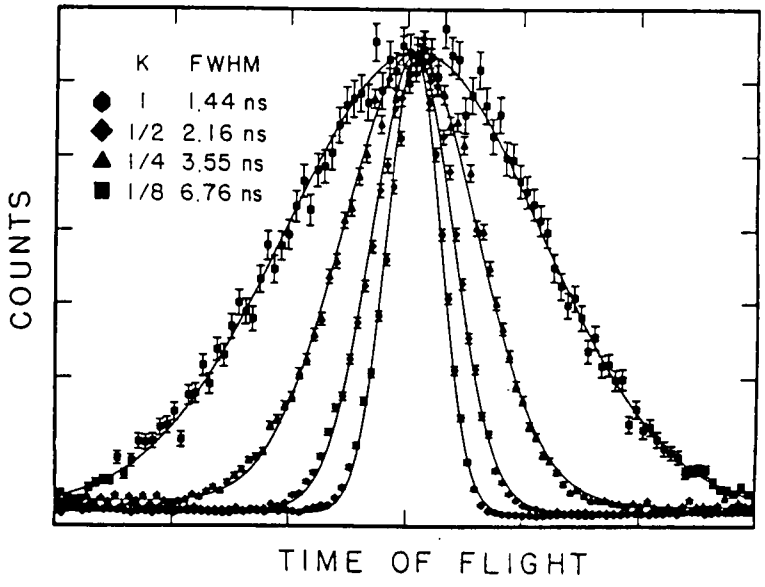


Figure 4.6 Ar^{4+} TOF peaks obtained using scaled spectrometer electric fields corresponding to κ = 1, 1/2, 1/4, and 1/8. Average initial ion energy can be deduced from the increase in peak width (Chapter 3).

Figures 4.7 and 4.8 are TOF spectra of neon and argon recoil ions, respectively, produced in collisions of 23 MeV Cl^{5+} with dilute gas targets, and detected in coincidence with electrons ejected during the ionization event. The charge-state distributions obtained in this manner did not peak at charge state one, as do total recoil-ion production cross sections (Cocke, 1979). Instead, charge state two is maximum for each spectrum. Two primary factors contributed to this shift in observed charge states: (1) electron capture was a likely mechanism for production of charge state one ions; (2) electron detection efficiency was not 100%, so it was thus more probable that an

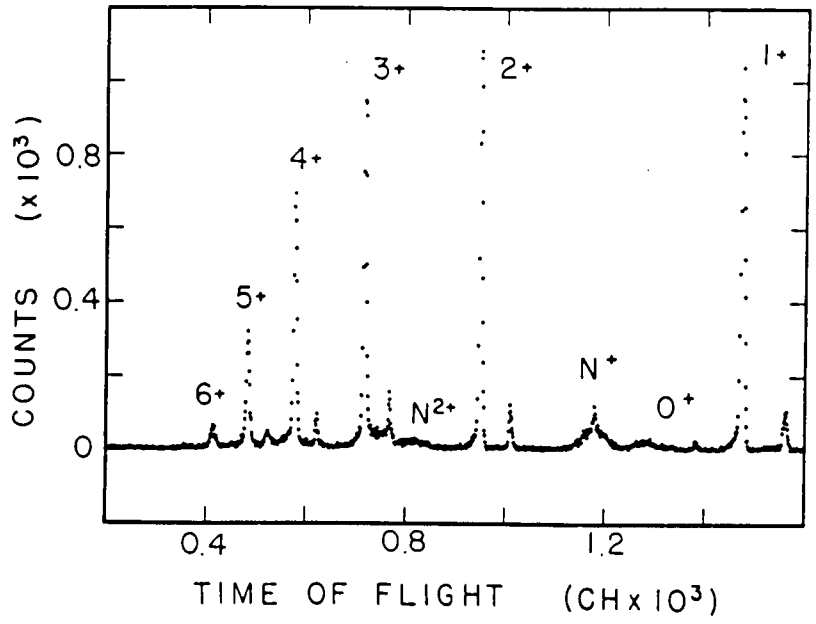


Figure 4.7. Neon recoil-ion charge-state distribution created by an incident 22.5 MeV Cl^{4+} beam and observed in coincidence with electrons ejected during ionization.

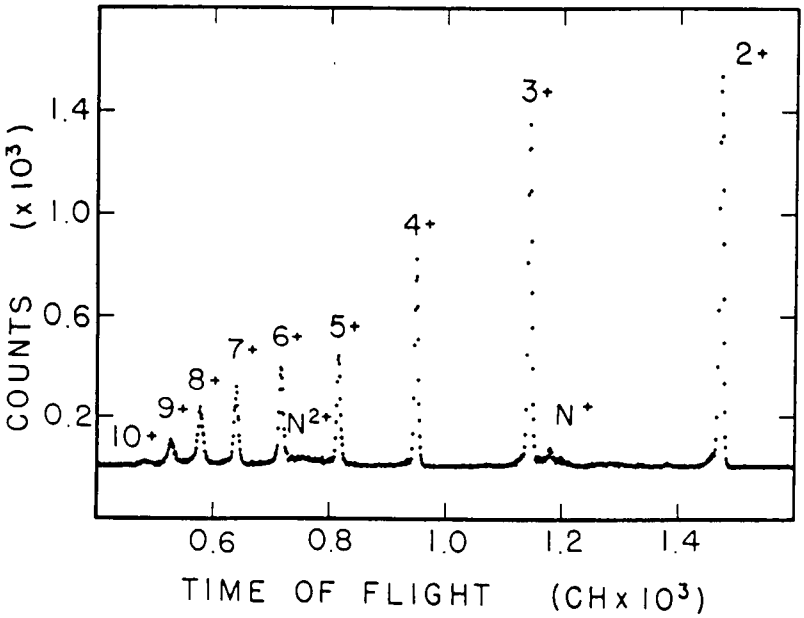


Figure 4.8. Argon recoil-ion charge-state distribution created by an incident 23 MeV Cl^{5+} beam and observed in coincidence with electrons ejected during ionization.

electron-ion coincidence was registered when more electrons were available for detection (e.g., charge states three and above).

Figure 4.9 displays argon charge-state distributions obtained in coincidence with projectile ions. As before, these are not representative of total recoil-ion production cross sections; all are shifted to higher charge states. The most abundant charge states for projectile-single-, double-, and triple-electron loss are argon charge states three, four, and six, respectively. These shifts to higher charge states can be attributed to harder collisions involving smaller impact parameters (b).

The TOF data files obtained at ORNL were transferred via a direct serial interface bus from the LeCroy 3500 to a MicroVax II computer, converted to the data format used at SSRL, and fitted to Pearson Type VII functions as described above. One exception is worth noting: although most all of the peaks were described well by Gaussians, the χ^2 minimization procedure (Bevington, 1969) applied to some higher-charge-state peaks resulted in artificially broadened Gaussians due to the substantial nonlinear background. Permitting a Lorentzian component in the fitting function allowed extraction of accurate widths by better modeling the background. The nonlinear backgrounds observed in some cases are believed to arise from a broad distribution of contaminant ions resulting from Coulomb explosions of ionized molecular background gases (Carlson, 1972; Short, 1987). It is also possible that some charge exchange between the higher charge states and the neutral background gas occurred as recoil ions traversed the gas cell, thereby producing a low level background in the TOF spectra.

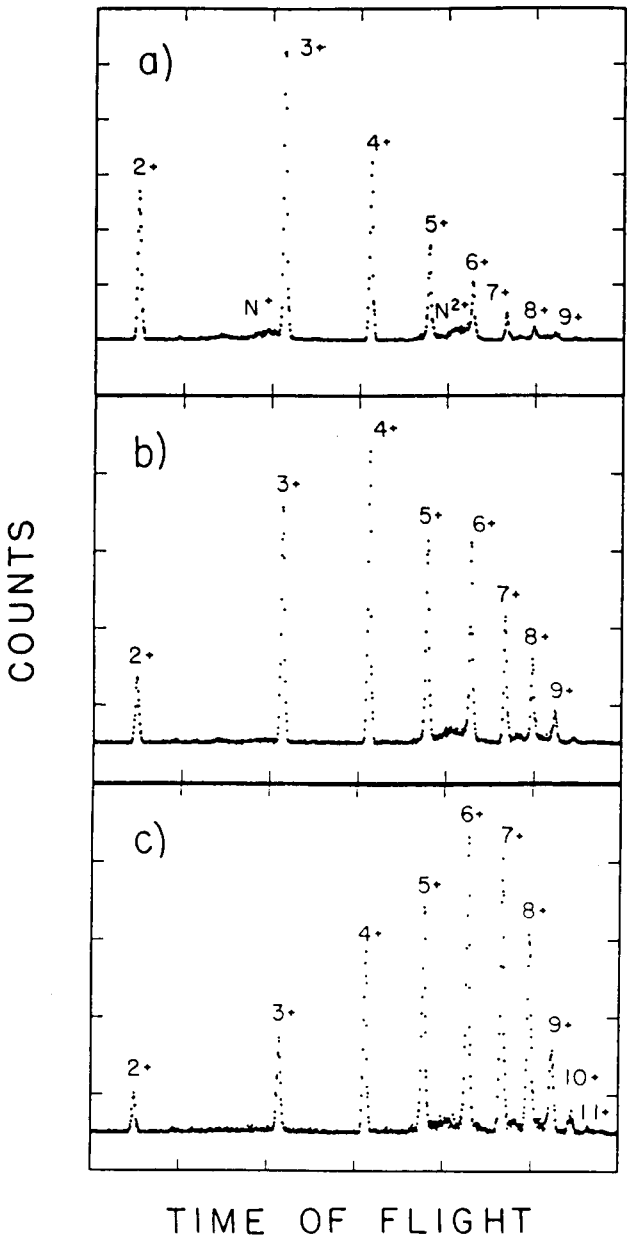


Figure 4.9 Argon recoil-ion charge-state distributions created by an incident 23 MeV Cl^{+5} beam and observed in coincidence with exiting projectile charge state. (a) Projectile-one-electron loss; (b) projectile-two-electron loss; and (c) projectile-three-electron loss. Times scales are reversed.

The electron-projectile coincidence data were analyzed to determine the effect of different spectrometer electric fields on the coincident-electron-timing reference. The spectrometer electric fields were assumed to have negligible effect on the incident fast-beam trajectory, and thus the projectile-ion flight time. The primary peak in each spectrum was fitted to a Gaussian function to determine how the timing reference varied as spectrometer fields were changed. Figure 4.10 displays the slight linear dependence of $(FWHM)^2$ on the inverse of electric field scaling parameter $(1/\kappa)$ for values of κ from 1 to 1/3. For the $\kappa = 1/6$, however, the peak width nearly doubled; consequently, all recoil ion data obtained in coincidence with electrons for $\kappa = 1/6$ were omitted from further analysis. These increases in peak width

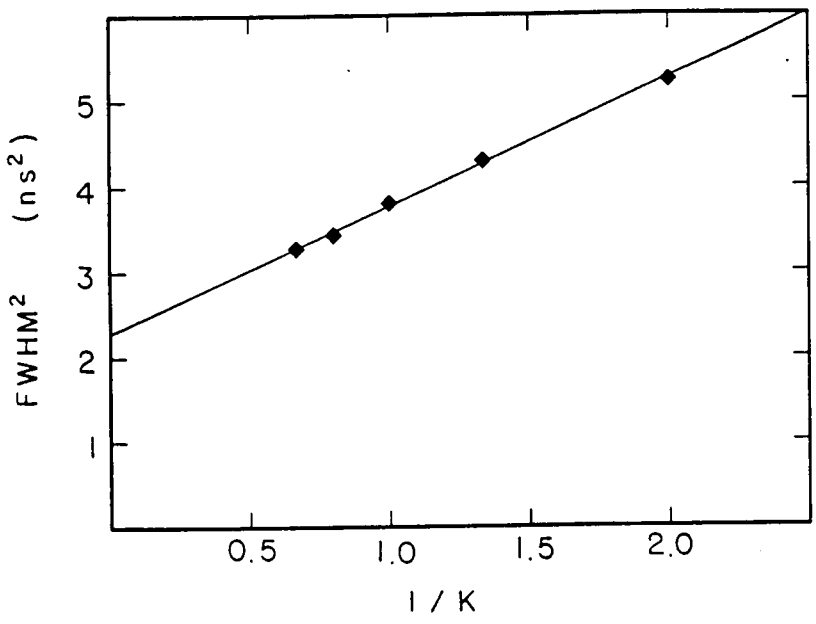


Figure 4.10. Dependence of TOF peak width on spectrometer electric field scaling parameter (κ) for electrons detected in coincidence with projectile ions.

were attributed to the greater influence of stray electric and magnetic fields at lower values of kappa.

The typical electron-projectile peak FWHM was about 2 ns, indicating a variation in timing reference from each source (electrons or projectile ions) of less than 2 ns, in contrast to the nearly constant reference at SSRL (<1 ns). Variations in electron flight times, as well as in electron and projectile-ion detector output pulses, were considered to be the major factors contributing to changes in the timing references.

Determination of Recoil Energy

In order to determine average energies ($\bar{U}_o$) for ions produced in each experiment, the FWHM (ΔT) of the TOF peaks for each charge state were fitted to the functional form of Equation (3.11), and deduced from the fitted parameter (γ) using Equation (3.12), which are both repeated here for convenience.

$$(\Delta T)^2 = \alpha + \beta/(q\kappa) + \gamma/(q\kappa)^2 \tag{3.11}$$

$$\bar{U}_o = \frac{\gamma(\varepsilon_s)^2}{(1.02)^2(8m)} \tag{3.12}$$

Least squares fitting routines for polynomials (Bevington, 1969) were used in a FORTRAN program in order to obtain the fitted parameters α, β, and γ.

The recoil energies of ions produced by photoionization (SSRL) were found to have at most a weak dependence on ion charge state. The major contribution to ion recoil energy was believed to be from

primary photoelectron and Auger electron ejection, since the electron kinetic energies are typically much greater for these processes, than for secondary Auger transitions or electron shake-off. Therefore, data for all charge states were fitted together to obtain a charge-state averaged $\bar{U}_o$ for each gas. Figure 4.11 shows the universal fits for neon, argon, krypton, and xenon ions produced by inner-shell photoionization. The essential appropriateness of Equation 3.11, as well as the weak recoil-energy dependence on charge state, are both supported by the clustering of the data about quadratic curves.

Table 4.1 contains the fitted values of β for each gas; values of $\bar{U}_o$ derived from fitted values of γ are presented in Chapter 5. The values of α, β, and γ were obtained in the following manner. Quadratic fits were performed in which all three fit parameters were allowed to float. The values of the constant term (α) were found to cluster around zero, corroborating the good timing resolution claimed. These values were averaged giving $\bar{\alpha} = 0.06 +/- 1.14\ ns^2$, and then $\bar{\alpha}$ was used in new fits in order to obtain final values of β and γ. The similarity of β values, when normalized (Appendix A) by dividing by the mass of each gas, is expected from the model upon which Equation 3.11 is based, since field fringing and space focusing (Chapter 3) should be independent of gas type. Errors in β and γ, and consequently $\bar{U}_o$, were derived from the fits through the technique of propagation of errors described by Bevington (1969).

Recoil energies of ions produced by ion impact were assumed to depend strongly on recoil-ion charge state, since the major contribution to recoil energy was believed to be the Coulomb repulsion

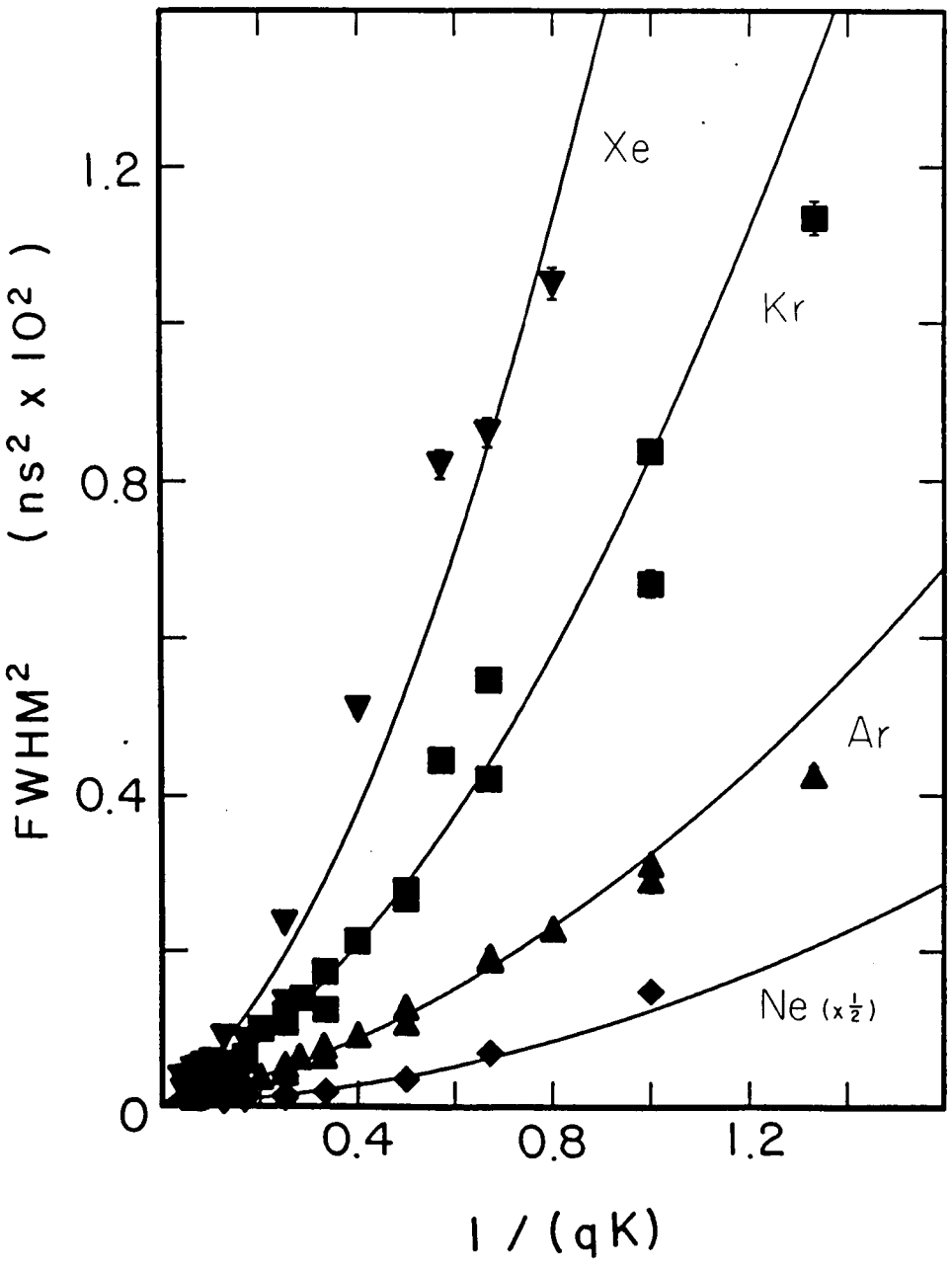


Figure 4.11. Quadratic fits of TOF peak widths used to determine recoil energies of neon, argon, krypton, and xenon ions produced by inner-shell photoionization. The parameter κ is an electric field scaling parameter and q is ion charge state.

Table 4.1. Linear (β) terms obtained from quadratic fits of TOF peak widths for ions produced by inner-shell photoionization. Also shown are the mass normalized linear terms β/m. Error bars (in parentheses) correspond to one standard deviation.

Gas	β	β/m
Ne	6.5 (8.4)	0.33 (0.42)
Ar	14 (9.4)	0.37 (0.23)
Kr	32 (8.5)	0.38 (0.10)
Xe	49 (17)	0.37 (0.13)

between the projectile and ionized target atom. Therefore, the FWHM data for each charge state were fitted separately to Equation (3.11). A small correction was subtracted from each $(\Delta T)^2$ data point for the electron-coincident data, thereby deconvoluting the changes in timing reference when spectrometer electric fields were varied (Figure 4.10). This linear correction affected only the fitted parameter β, but not α and γ, and thus had no effect on derived recoil energies.

Figure 4.12 displays the quadratic fits used to determine recoil energies of argon ions detected in coincidence with electrons. The recoil energy dependence on recoil-ion charge state is demonstrated by the increasing importance of the fitted quadratic term with increasing charge state. Figures 4.13 and 4.14 are examples of quadratic fits used to determine recoil energies of neon ions and argon ions,

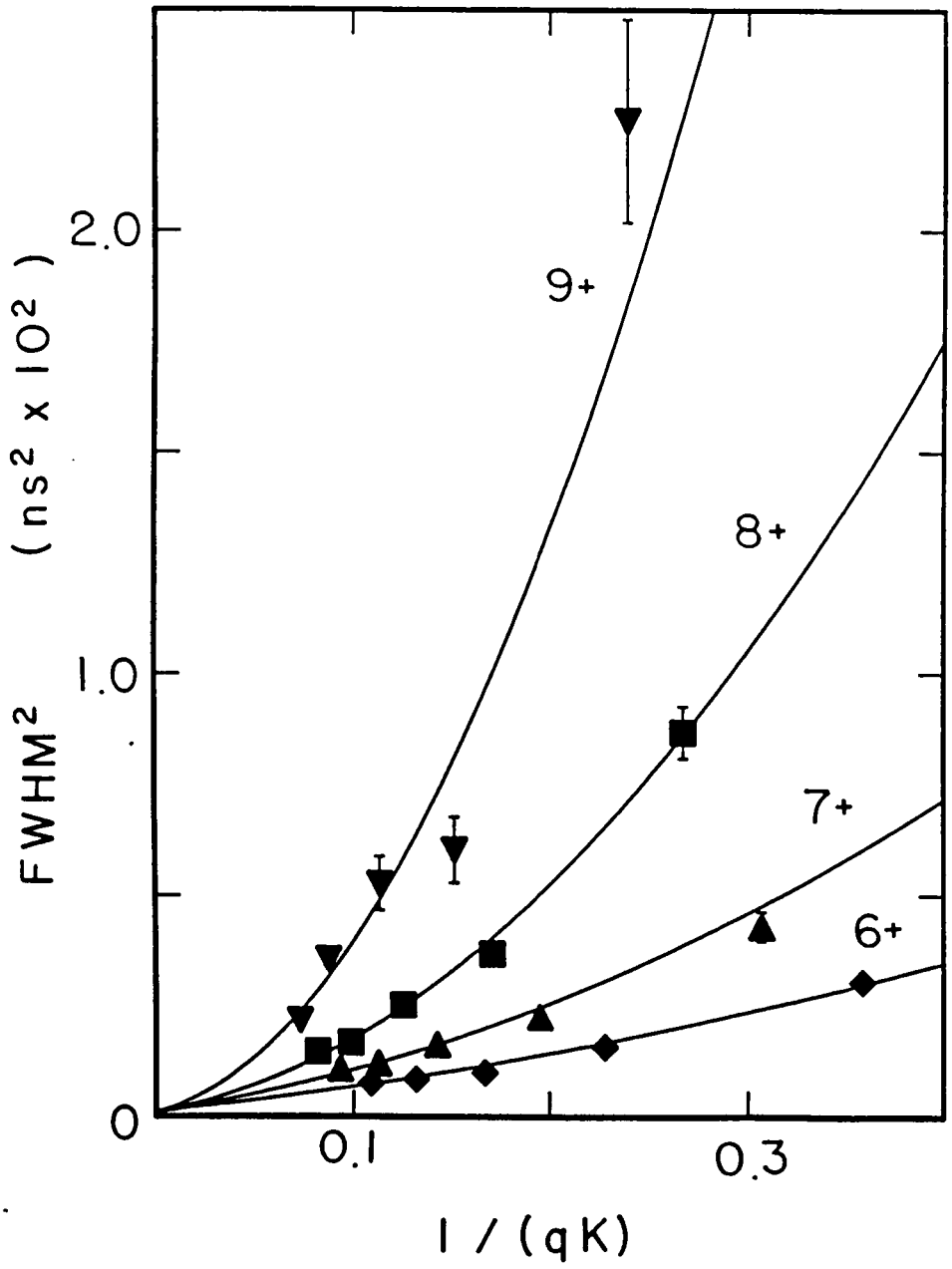


Figure 4.12. Quadratic fits of TOF peak widths used to determine recoil energies of argon ions produced by an incident 23 MeV Cl^{+5} beam and detected in coincidence with electrons. The parameter κ is an electric field scaling parameter and q is ion charge state.

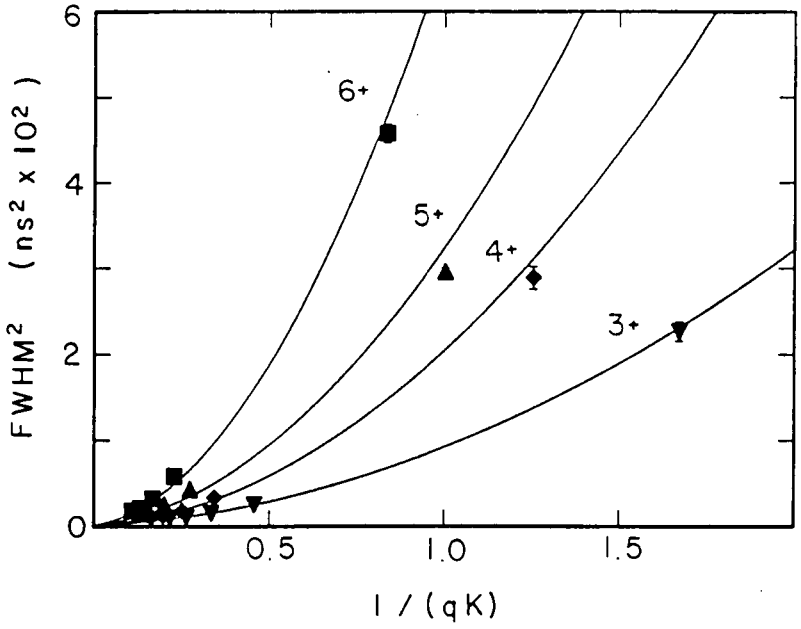


Figure 4.13. Quadratic fits of TOF peak widths used to determine recoil energies of neon ions produced by an incident 22.5 MeV Cl^{4+} beam and detected in coincidence with scattered Cl^{8+} projectile ions. The parameter κ is an electric field scaling parameter and q is ion charge state.

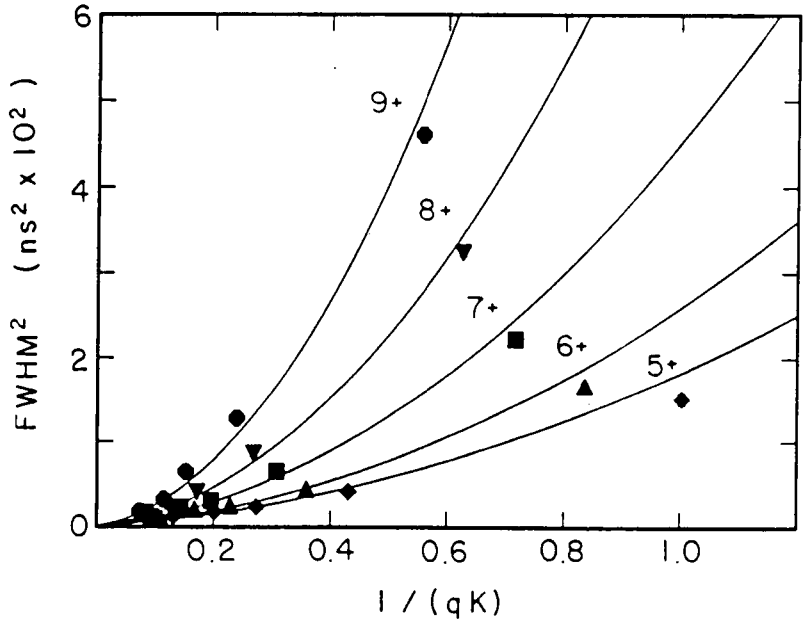


Figure 4.14. Quadratic fits of TOF peak widths used to determine recoil energies of argon ions produced by an incident 23 MeV Cl^{5+} beam and detected in coincidence with scattered Cl^{8+} projectile ions. The parameter κ is an electric field scaling parameter and q is ion charge state.

respectively, detected in coincidence with exiting projectile ions. The strong dependence on recoil-ion charge state is again evident.

Since data for each charge state for each gas were fitted separately, the quadratic curves were obtained from at most six data points, in contrast to the SSRL data in which all charge states were fitted together. Consequently, in order to assure a physically reasonable constant term, α was constrained to be $(1\ ns)^2 \pm (1\ ns)^2$ denoting an electronic timing resolution typically less than 2 ns.

The linear terms (β) derived from these fits were averaged for each charge state (Table 4.2), and then final values of γ were obtained from fits in which the linear terms were fixed to be these values. Since ions with higher recoil energies may experience more field fringing due to substantial transverse (to the TOF spectrometer axis) velocity components, the increase of β with recoil-ion charge state is not surprising. Statistical errors in the fitted quadratic term (γ) were derived from the fits through the technique of propagation of errors described by Bevington (1969), and correspond to one standard deviation. Recoil energies for charge states in each case were then determined using Equation (3.12) and are presented in Chapter 5.

Table 4.2 Average linear ($\bar{\beta}$) terms used for quadratic fits of TOF peak widths for recoil ions produced by swift-ion impact. Also shown are the mass normalized linear terms $\bar{\beta}/m$. Error bars (in parentheses) correspond to one standard deviation.

q	Ne		Ar	
	$\bar{\beta}$	$\bar{\beta}/m$	$\bar{\beta}$	$\bar{\beta}/m$
3	22 (7.9)	1.1 (0.4)	-	-
4	29 (7.2)	1.4 (0.4)	44 (16)	1.1 (0.4)
5	52 (15)	2.6 (0.8)	47 (13)	1.2 (0.3)
6	75 (22)	3.8 (1.1)	49 (15)	1.2 (0.4)
7	-	-	69 (29)	1.7 (0.7)
8	-	-	78 (42)	2.0 (1.0)
9	-	-	111 (80)	2.8 (2.0)

CHAPTER 5

RESULTS AND DISCUSSION

Inner-shell Photoionization (SSRL)

The measured average energies ($\bar{U}_o$) of neon, argon, krypton, and xenon ions produced by inner-shell photoionization with broad spectrum synchrotron radiation are listed in Table 5.1. Each measurement represents a weighted average over a distribution of ion energies (Chapter 3). Error bars correspond to one standard deviation, and are derived from the quadratic fits (Chapter 4) through standard techniques of propagation of errors (Bevington, 1969). Statistical uncertainties in the FWHM of each TOF peak contributed to these errors; furthermore, it is likely that the model through which TOF peak widths were deconvoluted in order to calculate ion energies (Chapter 3) is only an

Table 5.1 Measured and estimated average energies ($\bar{U}_o$) of inert gases following inner-shell photoionization with broad spectrum synchrotron radiation. Error bars (in parentheses) correspond to one standard deviation.

Primary Vacancy	Exp. $\bar{U}_o$ (eV)	Est. $\bar{U}_o$ (eV)
Ne (K)	0.11 (0.11)	0.11
Ar (K)	0.053 (0.073)	0.047
Kr (L)	0.073 (0.019)	0.032
Xe (M,L)	0.11 (0.042)	0.030

approximation of the true process. There may also be a dependence of ion energy on charge state for each gas, since more electrons are ejected for the higher charge states. However, the data suggest that this dependence is very weak (Chapter 4).

The corresponding estimated energies in Table 5.1 were derived from a simple model in which ion recoil energy was assumed to arise primarily from momentum conservation during photoelectron and primary Auger electron ejection. Ion recoil from secondary Auger transitions and electron shake-off was neglected, since the electron kinetic energies in these processes are typically much smaller. The model was simplified further by assuming that the distributions of photoelectron and Auger electron trajectories were isotropic.

Contributions from thermal energy, photoelectron ejection, and Auger electron ejection were added in quadrature to obtain the estimates of $\bar{U}_o$ in the following manner. Photoelectron energies were calculated for photoionization of the neon K-shell, argon K-shell, krypton L-shell, and xenon L-shell with 5 keV photons. The ion recoil energy necessary to conserve momentum during photoelectron ejection was then calculated for each gas. The ion recoil arising from the ejection of the most energetic Auger electron allowed, in the subsequent filling of each initial vacancy, was similarly calculated. These two contributions to recoil energy for each gas were added in quadrature with an estimated initial thermal energy of 0.025 eV to obtain total estimated energies.

The measured energies for each gas lie well within the range of the Maxwell-Boltzmann distribution of energies of the target gas at

room temperature. However, details of the modification of the original equilibrium distribution from the processes leading to multiple ionization are not known.

The higher neon energy can be, at least partially, attributed to high photoelectron velocity, since the neon K-edge lies far below the ~3 keV beryllium window cutoff of the ionizing radiation. Ion recoil during photoelectron ejection accounts for most of the estimated energy for neon in Table 5.1. Although the horizontally polarized synchrotron radiation gave rise to dipole photoelectron distributions that were peaked in the horizontal plane (Tseng et al., 1978; Southworth et al., 1983), components along the vertical TOF spectrometer axis contributed to the average ion kinetic energy measured. The increase in average energy with Z which was observed for argon, krypton, and xenon (Table 5.1) may be attributed to further ion recoil during the subsequent Auger processes which led to multiple ionization, since the average extent of ionization also increased with Z (Table 5.2).

Charge state fractions observed for neon, argon, krypton, and xenon following inner-shell photoionization with white light are listed in Table 5.2. The corresponding typical total ion production rates were ~200 Hz for neon, ~1 kHz for argon, ~2 kHz for krypton, and ~5 kHz for xenon. Since the maximum charge state observed for neon was 4+ and neon production rates were quite low, it does not appear that synchrotron-radiation inner-shell photoionization is an efficient means of producing highly charged neon ions. The production rates and abundance of high states of ionization for argon, krypton, and xenon, however, indicate that further studies of highly-charged ions produced

Table 5.2. Charge state fractions observed following inner-shell photoionization of inert-gas atoms with broad spectrum synchrotron radiation.

Primary Vacancy	Charge State (q) +2	+3	+4	+5	+6	+7	+8	+9	+10	+11	+12	+13
Ne (K)	0.56	0.28	0.17	-	-	-	-	-	-	-	-	-
Ar (K)	0.09	0.14	0.37	0.27	0.10	0.02	0.003	-	-	-	-	-
Kr (L)	-	0.07	0.22	0.23	0.26	0.17	0.05	-	-	-	-	-
Xe (M,L)	0.01	0.02	0.05	0.06	0.11	0.17	0.23	0.17	0.12	0.05	0.01	0.002

by this method is feasible. For example, the near thermal energies suggest that low-emittance beams of nearly monoenergetic multiply-charged ions could be extracted and used in very-low-energy atomic collision studies.

Furthermore, an increase in photon flux (and therefore ion production rates) is possible, since stored-electron beam current and energy were limited for the high-energy physics experiments which were simultaneously in progress. If the 54-pole wiggler line at SSRL is used with a 100 mA 3-GeV electron beam (instead of an 8-pole wiggler with a 10 mA 2-GeV electron beam) an increase of about two orders of magnitude in flux is achievable. With ion production rates of ~100 kHz, precision spectroscopy experiments of very slow highly-charged ions may be practical.

Table 5.3 contains the average charge states ($\bar{q}$) (Chapter 4) for neon, argon, krypton, and xenon following photoionization of inner shells as designated. Comparable measurements using x-ray tubes and filters (Carlson et al., 1966; Lightner et al., 1972), and more recent results using monochromatic x rays from the Photon factory synchrotron storage ring (Tonuma et al., 1987) are also included. The xenon distribution obtained using white light in the present experiment has been omitted from Table 5.3, since the broad spectral range of radiation permitted photoionization above, below, and interleaving the xenon L-edges, making interpretation and comparison of $\bar{q}$ difficult.

The present $\bar{q}$ results for K-shell photoionization of neon and argon agree well with those of Carlson and collaborators, yet there are discrepancies for photoionization above the L_1-edges of krypton and xenon. The krypton measurements of Lightner et al. and the xenon measurements of Tonuma et al., however, agree quite well with those presented here. Carlson et al. (1966) noted that properties of their mass spectroscopic equipment made data acquisition less reliable for low charge states, providing a possible explanation for some of the discrepancies. The dramatic shift that Carlson et al. observed when L_1-shell vacancies were possible, however, cannot be explained solely by their inefficiency of low-charge-state detection, since agreement with the present results and with those of Tonuma et al. is better for photoionization below the L_1 threshold.

Consideration of the Coster-Kronig yields (Chen et al., 1981) for transfer of an L_1 vacancy to the L_2-subshell ($f_{12} = 0.196$) and L_3-subshell ($f_{13} = 0.328$), indicate that ~52% of L_1 vacancies are

Table 5.3. Average charge state ($\bar{q}$) observed following inner-shell photoionization of inert-gas atoms. Energy of monochromatized x rays (in eV) is indicated in parentheses.

Deepest Vacancy	Average Charge State ($\bar{q}$) Present	Carlson[1]	Lightner[2]	Tonuma[3]
Ne (K)	2.3 (white)	2.3	2.2 (5400)	-
Ar (K)	4.2 (white)	4.2	4.1 (5400)	-
Kr (L_1)	5.4 (white)	6.7	5.4 (5400)	-
Xe (L_1)	7.8 (5475)	9.1 (8400)	-	7.74 (5800)
Xe (L_2)	7.7 (5400)	-	-	7.65 (5450)
Xe (L_3)	7.5 (5050)	7.4 (4960)	-	7.45 (5100)
Xe (M)	6.2 (4750)	6.5 (1500)	-	6.01 (4500)

[1]Carlson, T. A., W. E. Hunt, and M. O. Krause, 1966, Phys. Rev. **151**, 41.

[2]Lightner, G. S., R. J. Van Brunt, and W. D. Whitehead, 1971, Phys. Rev. A **4**, 602.

[3]Tonuma, T., A. Yagishita, H. Shibata, T. Koizumi, T. Matsuo, K Shima, T. Mukoyama, and H. Tamara, 1987, J. Phys. B **20**, L31.

filled in this manner. According to partial photoionization cross sections of the L-subshells (McMaster, 1969), L_1 vacancies are created roughly a third of the time by x rays with energy above the L_1-edge, leading to an estimated shift of ~0.15 in $\bar{q}$ as L_1 photoionization becomes energetically possible, thus lending support to the present results (0.1) and those of Tonuma et al. (0.11).

Swift-Ion Impact (ORNL)

Average energies (Chapters 3 and 4) of neon and argon ions produced in single collisions of fast chlorine ions with dilute gas targets are listed in Table 5.4., and displayed graphically for argon in Figure 5.1. Measured energies are represented here by $\bar{E}_R$ instead of $\bar{U}_o$ as above, because initial thermal energy (which is an appreciable fraction of the final energies of ions produced by photoionization) is usually negligible when compared with recoil energy arising from the collision process. These measurements (Table 5.4) were obtained for ions detected in coincidence with electrons ejected during ionization; incident beam energies and charge states are designated in each case.

The measured energies for the higher charge states are up to 2 orders of magnitude greater than those for ions produced by photoionization listed in Table 5.1. The error bars are statistically derived from the quadratic fits (Chapter 4), and correspond to one standard deviation. They are typically larger than corresponding estimated errors for similar measurements at SSRL, and are believed to arise from fluctuations of projectile beam position within the gas cell, in addition to the sources of error discussed above for the SSRL measurements. Furthermore, the timing references used at ORNL were not

Table 5.4. Average recoil-ion energies ($\bar{E}_R$) of neon and argon ions produced in collisions of fast chlorine ions with dilute gas targets. Energies and charge states of incident projectile beams are noted in parentheses. Error bars (in parentheses) correspond to one standard deviation.

q	Ne (Cl^{+4}) (22.5 MeV)	Ar (Cl^{+5}) (18 MeV)	(23 MeV)	(27.6 MeV)[a]	(27.6 MeV)[b]	(33 MeV)
3	<0.2	-	-	-	-	-
4	<0.2	<0.2	<0.2	<0.2	<0.2	<0.2
5	0.2 (0.3)	<0.2	<0.2	<0.2	<0.2	<0.2
6	2.6 (0.8)	0.4 (0.2)	0.3 (0.2)	0.1 (0.3)	0.3 (0.2)	0.2 (0.2)
7	-	1.2 (0.4)	0.8 (0.7)	0.6 (0.6)	0.8 (0.5)	0.4 (0.3)
8	-	4.1 (0.7)	2.7 (1.1)	1.8 (1.0)	2.3 (0.8)	1.5 (0.9)
9	-	13.9 (1.6)	8.2 (2.6)	7.2 (2.2)	6.8 (1.9)	5.0 (1.1)

[a] September, 1986. [b] October, 1986.

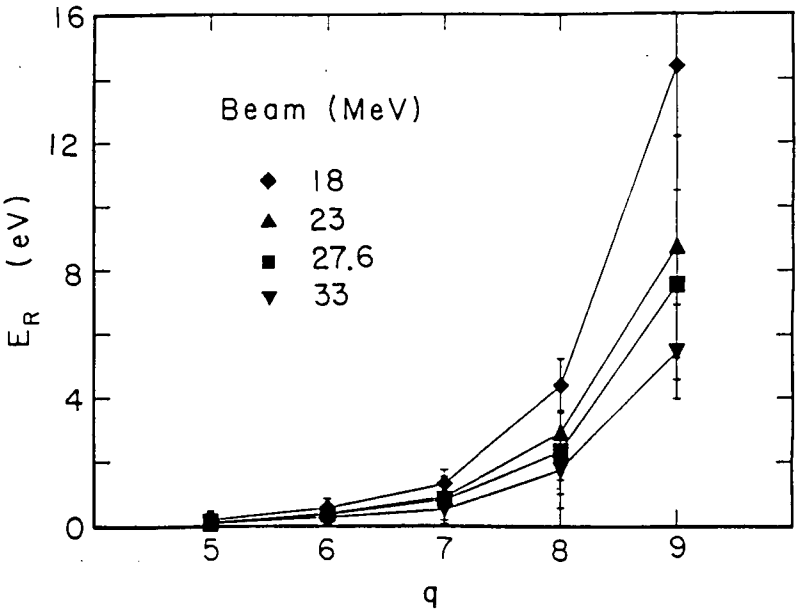


Figure 5.1. Average recoil energies ($\bar{E}_R$) of argon ions produced by 18, 23, 27.6, and 33 MeV Cl^{5+} ions plotted vs. recoil-ion charge state.

as stable as the RF reference used at SSRL. Values for some low charge states were not included in Table 5.4, since poor statistics (Chapter 4) prohibited extraction of recoil energies for these ions.

The dependence of $\bar{E}_R$ on projectile-beam energy (E_p) is steeper than the ($1/E_p$) suggested by earlier estimates (Equation 2.2). The measurements are, however, consistent with a $1/E_p$ dependence within error bars. The dramatic increase in recoil energy for Ar^{9+} observed for each incident beam energy can be at least partially understood by shell effects, since the removal of nine electrons requires breaking the L-shell of argon, thereby implying that collisions at much smaller impact parameters are required.

Average recoil energies ($\bar{E}_R$) determined in coincidence with exiting projectile charge states (r) were found to have a strong dependence on r as well recoil-ion charge state q. Figures 5.2 and 5.3 display this steep dependence for 22.5 MeV Cl^{+4} incident on neon, and 23 MeV Cl^{+5} incident of argon, respectively. The rapid variation suggested the possibility of relatively sharp definition of characteristic average impact parameters ($\bar{b}$) for coincident projectile and target ionization. A model connecting $\bar{E}_R$ and $\bar{b}$ was needed in order to realize this possibility.

Although the collision processes of concern here are complex many-body problems, a model based on two-body kinematics was assumed to serve as a useful approximation for connecting $\bar{E}_R$ and $\bar{b}$, since the electron-to-nuclei mass ratios are $\sim 10^{-5}$.

An elastic screened-Coulomb scattering model was used to determine the center-of-mass projectile scattering angle (Θ_m) by evaluating the classical deflection function (Goldstein, 1980) in two parts:

$$\Theta_{cm} = \pi - b \sum_{i=1}^{2} \int_{\rho_o}^{\infty} \frac{d\rho}{\rho^2 \left[1 - \frac{b^2}{\rho^2} - \frac{V_i(\rho)}{E_{cm}} \right]^{1/2}} \qquad (5.1)$$

where b is the impact parameter, E_{cm} is the total center-of-mass energy of the system, ρ is the internuclear separation (with ρ_o the distance of closest approach), and V_i is the interatomic potential described below.

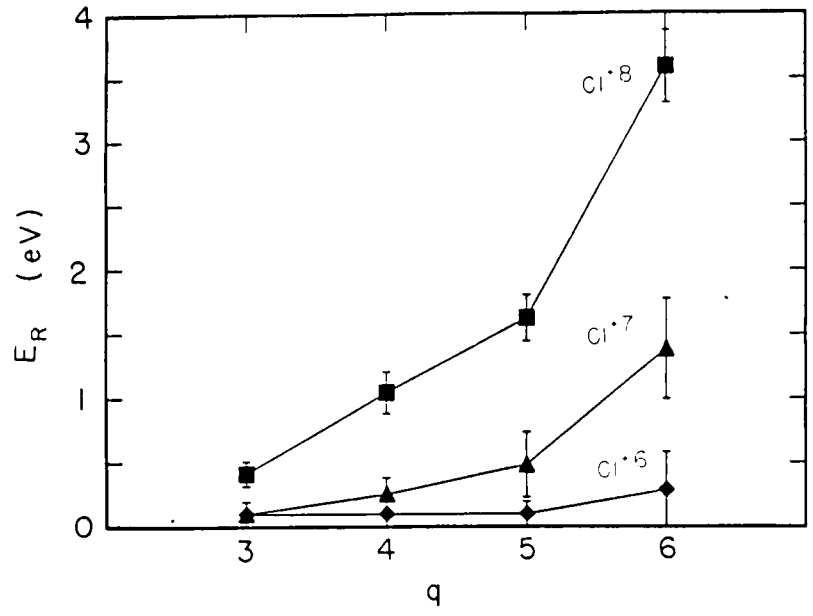


Figure 5.2. Average recoil energies ($\bar{E}_R$) of neon ions produced by 22.5 MeV Cl^{4+} ions and detected in coincidence with exiting projectile-ion charge states.

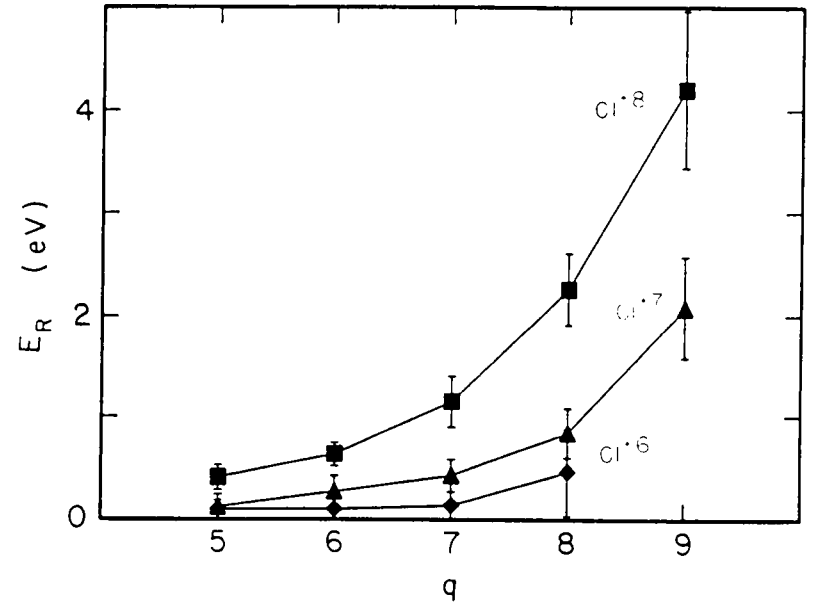


Figure 5.3. Average recoil energies ($\bar{E}_R$) of argon ions produced by 23 MeV Cl^{5+} ions and detected in coincidence with exiting projectile-ion charge states.

For the first half of the collision, the target was assumed to be neutral, thus giving a non-zero interatomic potential V_1 only when the internuclear separation (ρ) was small enough that the target nucleus was no longer fully screened by the electron charge cloud. The interatomic potential from this point was approximated by the potential of the bare target and projectile nuclei, reduced as a function of ρ by the universal screening function of Ziegler et al. (1985).

For the second half of the collision, the interatomic potential V_2 was approximated by the greater of the following: (1) the potential of the bare target and projectile nuclei again reduced by the universal screening function (Ziegler et al., 1985); (2) the unscreened Coulomb potential for the final charge states of the projectile (r) and target (q).

The energy transfer to the target nucleus (E_R) was then calculated as a function of Θ_{cm} using energy and momentum conservation (Ziegler, 1985),

$$E_R = 4E_p \frac{(M_p M_q)}{(M_p + M_q)^2} \sin^2 \frac{\Theta_{cm}}{2} \qquad (5.2)$$

where M_p and M_q are the respective projectile and target masses, and E_p is the incident projectile energy in the laboratory frame. Hence, values of $\bar{b}$ were inferred from measured values of $\bar{E}_R$ using Equations 5.1 and 5.2. Figure 5.4 displays the relationship between E_R and b as calculated for 23 MeV Cl^{+5} + Ar → Cl^{+8} + Ar^{+q} using: (1) the present method described above; (2) Equation 2.2 derived from classical-trajectory Monte Carlo (CTMC) calculations by Olson (discussed in

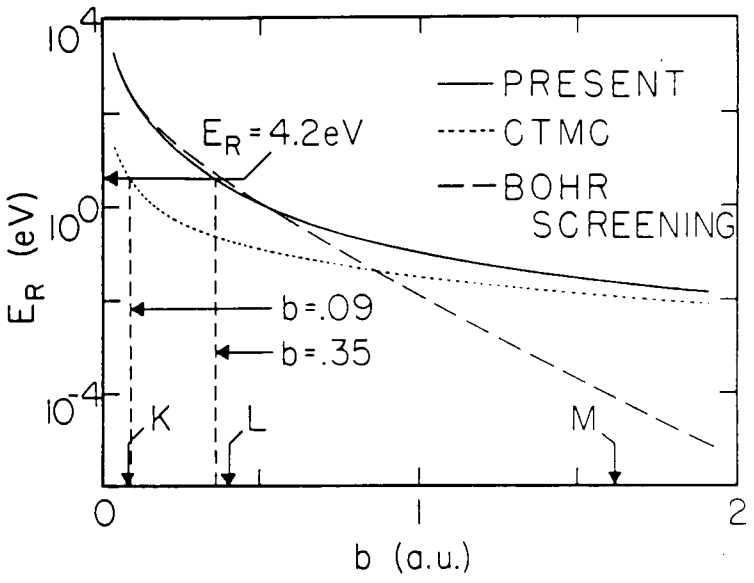


Figure 5.4. Ar^{9+} recoil energies as a function of impact parameter for 23 MeV Cl^{5+} + Ar → Cl^{8+} + Ar^{9+} for the present calculation (see text), a CTMC model[1], and Bohr screening. Indicated are measured recoil energy, corresponding impact parameters, and Hartree-Fock expectation values of neutral Ar K, L, and M shell.

[1]Schlachter et al., 1982, Phys. Rev. A **26**, 1373.

Chapter 2); and (3) a Bohr screening model for neutral projectile and target atoms. The measured recoil energy for Ar^{+9} is indicated along with corresponding impact parameters for methods (1) and (2). In the present model the measured value of $\bar{E}_R \cong 4.2$ eV for $(r,q) = (8,9)$ corresponds to $\bar{b} \cong 0.35$ a.u., whereas the results from CTMC calculations imply a value $b \cong 0.09$ a.u. Since this final state can only be formed by ionization from the L-shells of both target and projectile, the Hartree-Fock neutral target L-shell expectation value of 0.38 a.u. is consistent with the present results. Table 5.5 lists the measured values of $\bar{E}_R$ for recoil ions detected in coincidence

with exiting projectile charge states, along with corresponding calculated average impact parameters ($\bar{b}$). The values of $\bar{b}$ are considered to be representative of the impact-parameter dependent probability distribution for each multiple-ionization process; however the weighting factors for the averaging process are unknown.

These recoil-energy measurements offered an opportunity to explore the present applicability of the approximately half-Rutherford scattering formula (Equation 2.2, repeated below) derived by Olson (Schlachter et al., 1982) from CTMC calculations for collisions of highly stripped uranium ions with inert-gas atoms.

$$E_R \text{ (in eV)} \cong (4\times10^{-4})p^2q^2/(M_t E_p b^2) \qquad (2.2)$$

The two modes of data acquistion during the present experiment suggest two limiting cases. During the first mode, recoil ions were detected in coincidence with electrons, thus providing no information concerning the final projectile charge state. Therefore, the incident projectile charge state (p) must be used in Equation 2.2 for the recoil-ion energies in Table 5.4. During the second mode, recoil ions were detected in coincidence with final projectile charge states, thus allowing a fairer test of Equation 2.2 by replacing p with the exiting projectile charge state (r) for recoil-ion energies in Table 5.5.

Figure 5.5 displays plots of $\log(\bar{E}_R)$ vs. $\log(pq)$ for argon recoil energies determined in coincidence with electrons (Table 5.4) in which the least squares linear fits suggest a power law of the form $E_R \propto (pq)^n$, with $n \cong 10$, instead of the $(pq)^2$ dependence of Equation 2.2. Such a

Table 5.5. Average energies ($\bar{E}_R$) and impact parameters ($\bar{b}$) for neon and argon recoil ions detected in coincidence with exiting projectile ions Cl^{r+}. Incident beam energies of 22.5 MeV (Cl^{4+}), 23 MeV (Cl^{5+}), and 27.6 MeV (Cl^{5+}) were used. Error bars (in parentheses) correspond to one standard deviation.

q	r	Ne (22.5 MeV)		Ar (23 MeV)		Ar (27.6 MeV)	
		$\bar{E}_R$ (eV)	$\bar{b}$ (au)	$\bar{E}_R$ (eV)	$\bar{b}$ (au)	$\bar{E}_R$ (eV)	$\bar{b}$(au)
4	8	1.04 (0.16)	0.45	-	-	-	-
5	6	0.10 (0.29)	0.71	-	-	-	-
5	7	0.48 (0.25)	0.51	-	-	-	-
5	8	1.62 (0.18)	0.40	0.41 (0.12)	0.55	0.21 (0.09)	0.61
6	6	0.29 (0.38)	0.59	-	-	-	-
6	7	1.38 (0.39)	0.41	0.27 (0.15)	0.64	<0.2	>0.67
6	8	3.59 (0.28)	0.34	0.63 (0.12)	0.54	0.35 (0.12)	0.58
7	6	-	-	<0.3	>0.60	<0.3	>0.59
7	7	-	-	0.42 (0.16)	0.58	<0.4	>0.6
7	8	-	-	1.14 (0.25)	0.48	0.71 (0.21)	0.50
8	6	-	-	0.46 (0.42)	0.57	0.40 (0.35)	0.56
8	7	-	-	0.84 (0.24)	0.50	0.47 (0.28)	0.55
8	8	-	-	2.26 (0.35)	0.41	1.43 (0.34)	0.43
9	7	-	-	2.08 (0.50)	0.42	1.66 (0.54)	0.42
9	8	-	-	4.20 (0.76)	0.35	2.74 (0.78)	0.37

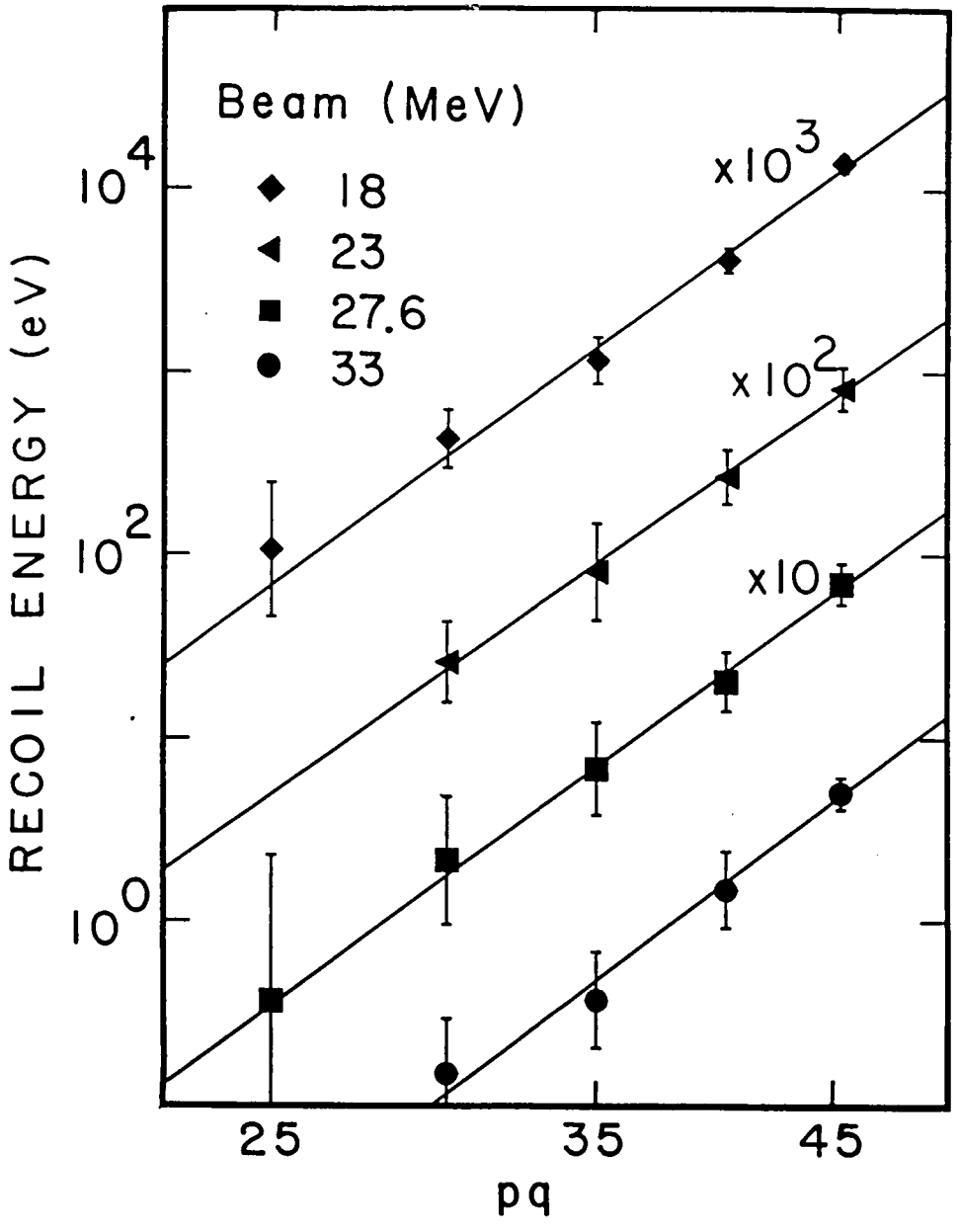


Figure 5.5. Argon recoil energy ($\bar{E}_R$) vs. product (pq) of incoming projectile charge and recoil-ion charge for beams of 18, 23, 27.6, and 33 MeV Cl^{5+}. Data have been fitted to straight lines and are shifted for clarity. Both scales are logarithmic. The 27.6 MeV data plotted are the average of the data in Table 5.4.

comparison, however, includes neither possible projectile stripping, nor the impact parameter (b) dependence of production cross sections for each charge state (Cocke, 1979) and the b^{-2} dependence predicted for E_R; creation of higher recoil-ion charge states is more probable at smaller impact parameters.

Figure 5.6 display similar plots of $\log(\bar{E}_R)$ vs. log(rq) for argon recoil energies determined in coincidence with exiting projectile charge states (Table 5.5). These recoil energies were found to cluster for values of (rq) independently of individual values of r and q. As above, the least squares linear fits imply a power law of form

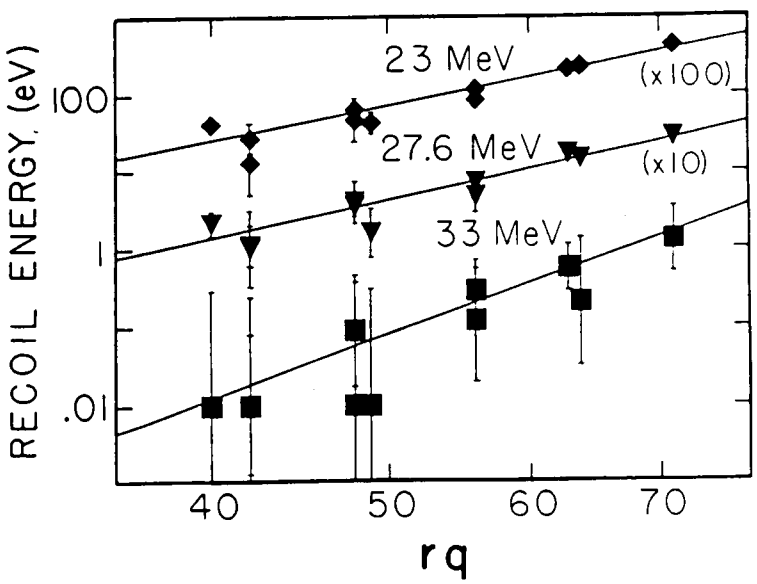


Figure 5.6. Argon recoil energy ($\bar{E}_R$) vs. product (rq) of final projectile charge and recoil-ion charge for beams of 23, 27.6, and 33 MeV Cl^{5+}. Data have been fitted to straight lines (snifted for clarity). Both scales are logarithmic.

$\bar{E}_R \propto (rq)^n$, but with $n \cong 5$ in this case (in similar fits for neon, $n \cong 3$). This dependence is still steeper than that ($n = 2$) predicted by Equation 2.2, suggesting that the effective charges seen by the target and projectile nuclei near closest approach may be of greater importance in these collisions than the asymptotic values q and r in determining E_R. In fact, if the effective target and projectile charges (12.6 and 11.9, respectively for b = 0.35 a.u.) obtained from Hartree-Fock calculations are used, Equation 2.2 yields a recoil energy of 2.8 eV, in contrast to the unrealistically low value of ~0.3 eV found using the asymptotic values (r,q).

The discrepancies between our results and those predicted by Equation 2.2 may be ascribed in part to a sudden collision condition not being met in the present experiment. The independent-particle (IP) model, upon which the CTMC calculations resulting in Equation 2.2 were based, requires that the collision be sufficiently sudden that the average binding energies assumed for electrons in each shell do not change during the course of the collision (Schlachter, 1982). Furthermore, screened Z's are not used in a description of the internuclear motion in the IP model, but rather are picked to optimize radial expectation values of the active electrons. The influence of Pauli excitation arising from overlapping projectile and target electron clouds is also neglected.

In order to investigate whether the energy deposition (ED) model (Russek, 1963), discussed in Chapter 2, may provide a key to understanding the dependence of $\bar{E}_R$ on r and q, the following approach was taken. The total excitation energy (Q) deposited into the

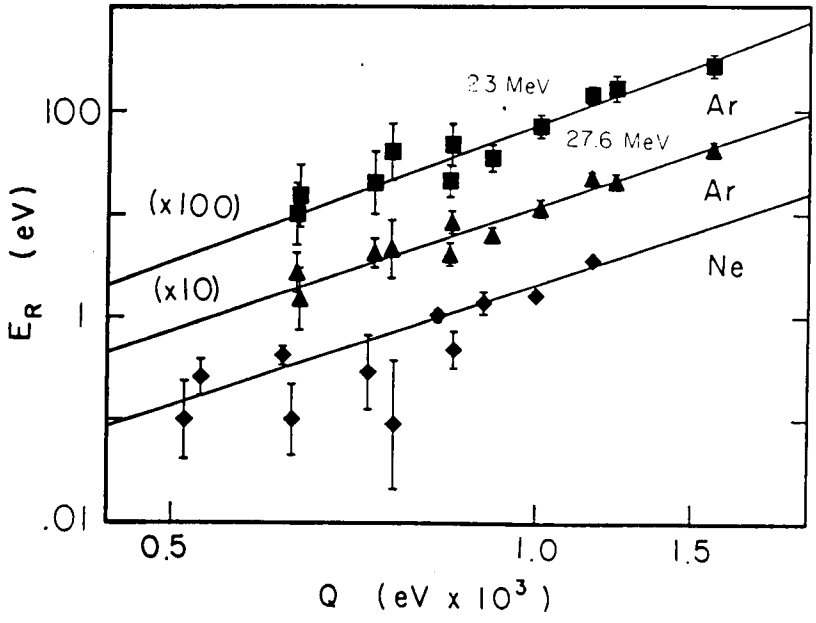


Figure 5.7. Recoil-ion energy ($\bar{E}_R$) vs. reaction energy (Q) for beams of 22.5 MeV Cl^{4+} incident on neon, and 23, 27.6 MeV Cl^{5+} incident on argon. Q values are estimated from ionization potentials. Data have been fitted to straight lines (shifted for clarity). Both scales are logarithmic.

collision system was estimated to be the total ionization potential of all electrons ejected for each reaction product pair (r,q). Figure 5.7 displays plots of $\log(\bar{E}_R)$ vs. $\log(Q)$ for neon and argon which also imply a power law $\bar{E}_R \alpha (Q)^n$, with $n \cong 3$, suggesting that it may be useful to further investigate the correlation between E_R and Q through definite impact parameter dependences of each.

CHAPTER 6

SUMMARY

Highly-charged ions were created by inner-shell photoionization of inert-gas atoms using intense synchrotron radiation, and also in collisions of fast (MeV) chlorine-ion beams with dilute inert-gas targets. Time-of-flight (TOF) techniques were used to investigate charge-state distributions, and measure average recoil energies for ions produced in each manner. High states of ionization (e.g., Ar^{6+}) were produced in each method, however, recoil energies of all ions produced by photoionization were found to correspond essentially to room temperature, while recoil energies of the higher-charge-state ions produced in ion-atom collisions were up to two orders of magnitude greater. Recoil-ion production rates were on the order of kHz in both experiments.

The ability to create highly-charged ions in a nearly room-temperature environment may allow interesting new experimental possibilities. Extraction of high-charge-state ions to form nearly monoenergetic beams of very-low-energy (<10 eV) ions with good angular definition appears possible. Tne development of such a Very Cold--or x-ray Vacancy Cascade--Ion Source (VCIS) would offer the potential of new angle-resolved atomic collision studies at very-low energies. Since synchrotron x rays can be focused to very small spot sizes (~100 μm in diameter), extremely high-brightness sources should be achievable. The pulsed nature of the excitation also lends itself naturally to the development of high-resolution coincidence and TOF experiments.

Precision spectroscopy experiments of unprecedented accuracy may also be possible. Spectroscopic studies of recoil ions produced in ion-atom collisions have permitted reductions in Doppler shifts and spreads typical in fast-beam approaches to this problem by three to four orders of magnitude in v/c (Sellin et al., 1977). The ability to produce very-low-energy highly-charged ions by synchrotron radiation should allow a further reduction by one- to two- orders of magnitude in v/c.

New knowledge concerning the dynamics of energetic ion-atom collisions was also gained from the investigations of recoil energies of ions produced by swift-ion impact. Impact parameters (b) characteristic of simultaneous target and projectile stripping were inferred from the measured average recoil-ion energies ($\bar{E}_R$), in collisions where both the recoil-ion and scattered-projectile-ion charge states were determined in coincidence. An elastic two-body screened-Coulomb scattering calculation was coupled with energy-momentum conservation to relate E_R with b for the various incident beam energies and exiting projectile and target charge states.

Recoil-ion energies were found to increase more steeply with total projectile and target ionization than suggested by a previous model (Schlachter et al., 1982), in which recoil energies were assumed to arise primarily from the Coulomb repulsion of the exiting charged projectile and ionized target atom. This steep dependence seems to indicate that the dominant factor determining final recoil-ion energy for very close collisions (b smaller than expectation values of intermediate or inner shells), is the Coulomb repulsion of the

partially-screened nuclei near closest approach. Understanding multiple ionization at a more fundamental level through further exploration of these collision parameters is desirable and believed to be feasible.

The appreciable cross sections measured for recoil-ion production in collisions of highly-stripped 15.5 MeV/u uranium projectiles with argon gas atoms (Ullrich et al., 1984; Kelbch et al., 1985) have led to a proposal for the development of a permanent recoil-ion source on a high-energy heavy-ion accelerator, or heavy-ion storage ring. Knowledge of recoil-ion energies should be useful in determining the ion-optical quality of low-energy beams from such parasitic ion sources, since spreads in beam energy and angular definition arising from recoil-ion energies may be appreciable.

LIST OF REFERENCES

LIST OF REFERENCES

Abramowitz, M., and I. A. Stegun, 1965, Handbook of Mathematical Functions, (Dover Publications, Inc., New York).

Bárány, A., G. Astner, H. Cederquist, H. Danared, S. Huldt, P. Hvelplund, A. Johnson, H. Knudsen, L. Liljeby, and K.-G. Rensfelt, 1985, Nucl. Instrum. Meth. **B9**, 397.

Bashkin, S. (ed.),1968, Beam-Foil Spectroscopy, (Gordon and Breach, New York).

Bevington, P., 1969, Data Reduction and Error Analysis for the Physical Sciences, (McGraw-Hill, New York).

Beyer, H. F., R. D. Deslattes, F. Folkmann, and R. E. LaVilla, 1985, J. Phys. B **18**, 207.

Beyer, H. F., R. Mann, F. Folkmann, and P. H. Mokler, 1982, J. Phys. B **15**, 3853.

Bienenstock, A., 1980, Nucl. Instrum. Meth. **172**, 13.

Bienenstock, A., and H. Winick, 1983, Physics Today **June**, 48.

Brown, M. D., J. R. Macdonald, P. Richard, J. R. Mowat, and I. A. Sellin, 1974, Phys. Rev. A **9**, 1470.

Carlson, T. A., 1975a, Radiat. Res. **64**, 53.

Carlson, T. A., 1975b, Photoelectron and Auger Spectroscopy, (Plenum, New York).

Carlson, T. A., W. E. Hunt, and M. O. Krause, 1966, Phys. Rev. **151**, 41.

Carlson, T. A., and M. O. Krause, 1965, Phys. Rev. **137**, A1655.

Carlson, T. A., and M. O. Krause, 1972, J. Chem. Phys. **56**, 3206.

Carlson, T. A., and C. W. Nestor, Jr., 1973, Phys. Rev. A **8**, 2887.

Chen, M. H., B. Crasemann, and H. Mark, 1981, Phys. Rev. A **24**, 177.

Church, D. A., H. M. Holzscheiter, R. A. Kenefick, C.-S. O, R. T. Short, S. D. Berry, S. B. Elston, M. Breinig, R. DeSerio, I. A. Sellin, and B. Thomas, 1985, Appl. Phys. Lett. **47**, 330.

Church, D. A., K. W. Jones, B. M. Johnson, M. Meron, and I. A. Sellin, 1984, J. Phys. B **17**, L401.

Church, D. A., R. A. Kenefick, W. S. Burns, C.-S. O, R. Holmes, S. Huldt, S. Berry, M. Breinig, S. Elston, J.-P. Rozet, I. A. Sellin, D. Taylor, and B. Thomas, 1983, Phys. Rev. Lett. **51**, 1636.

Church, D. A., S. D. Kravis, M. Meron, B. M. Johnson, K. W. Jones, I. A. Sellin, C.-S. O, J. C. Levin, and R. T. Short, 1987, to be published.

Cocke, C. L., 1979, Phys Rev. A **20**, 749.

Cocke, C. L., R. DuBois, T. J. Gray, E. Justiniano, and C. Can, 1981, Phys. Rev. Lett. **46**, 1671.

Crasemann, B., and F. Wuilleumier, 1984, Physics Today **June**, 34.

Deslattes, R. D., H. F. Beyer, and F. Folkmann, 1984, J. Phys. B **17**, L689.

Elderton, W. P., and N. L. Johnson, 1969, Systems of Frequency Curves (Cambridge University Press, London).

Galileo Electro-Optics Corp., 1980, Data Sheet 6300.

Gerald, C. F., 1970, Applied Numerical Analysis, (Addison-Wesley, Redding).

Goldstein, H., 1980, Classical Mechanics, 2d, Ed., (Addison-Wesley, Redding).

González Lepera, C., M. Breinig, R. DeSerio, S. B. Elston, J. P. Gibbons, H.-P. Hülskötter, L. Liljeby, R. T. Short, and C. R. Vane, 1987, to be pubslished in Nucl. Instrum. Meth.

Gray, T. J., C. L. Cocke, and E. Justiniano, 1980, Phys. Rev. A **22**, 849.

Hamamatsu Co., 1983, Technical Manual RES-0795, and MCP Technical Data Sheet.

Hansteen, J. M., and O. P. Mosebekk, 1972, Phys. Rev. Lett. **29**, 1361.

Hastings, J. B., and V. O. Kostroun, 1983, Nucl. Instrum. Meth. **208**, 815.

Haugen, H. K., L. H. Andersen, P. Hvelplund, and H. Knudsen, 1982, Phys. Rev. A **26**, 1962.

Heitler, W., 1947, The Quantum Theory of Radiation, (Oxford University Press).

Holmes, R., et al., 1982, Bull. Am. Phys. Soc. **27**, 513.

Horbatsch, M., 1986, Z. Phys. D **1**, 337.

Hvelplund, P., L. H. Andersen, A. Bárány, H. Cederquist, J. Heinemeier, H. Knudsen, K. B. MacAdams, E. H. Nielsen, and J. Sorensen, 1985, Nucl. Instrum. Meth. **B9**, 421.

Hülskötter, H.-P., 1985, Diplomarbeit, Institut für Kernphysik, Westf.-Wilhelms Universität, Münster, unpublished.

Jones, K. W., B. M. Johnson, and M. Meron, 1983, Phys. Lett. **97A**, 377.

Justiniano, E., C. L. Cocke, T. J. Gray, R. D. DuBois, and C. Can, 1981, Phys. Rev. A **24**, 2953.

Justiniano, E., C. L. Cocke, T. J. Gray, R. DuBois, C. Can, W. Waggoner, R. Schuch, H. Schmidt-Böcking, and H. Ingwersen, 1984, Phys. Rev. A **29**, 1088.

Kelbch, S., J. Ullrich, R. Mann, P. Richard, and H. Schmidt-Böcking, 1985, J. Phys. B **18**, 323.

Kendall, M. G., 1948, The Advanced Theory of Statistics, Vol. II (Charles Griffin and Company, Ltd., London).

Kendall, M. G., and A. Stuart, 1943, The Advanced Theory of Statistics, Vol. I (Chargles Griffin and Company, Ltd., London).

Klein, H. A., S. Bashkin, B. P. Duval, F. Moscatelli, J. D. Silver, H. F. Beyer, and F. Folkmann, 1982, J. Phys. B **15**, 4507.

Krause, M. O., and T. A. Carlson, 1967, Phys. Rev. **158**, 18.

Krause, M. O., M. L. Vestal, W. H. Johnston, and T. A. Carlson, 1964, Phys. Rev. **133**, A385.

Levin, J. C., 1986, Ph.D. Dissertation, The University of Oregon, Eugene, unpublished.

Levin, J. C., R. T. Short, C.-S. O, H. Cederquist, S. B. Elston, J. P. Gibbons, I. A. Sellin, and H. Schmidt-Böcking, 1987, to be published.

Lightner, G. S., R. J. Van Brunt, and W. D. Whitehead, 1971, Phys. Rev. A **4**, 602.

Liljeby, L., ed., 1983, Phys. Scr. **T3**.

Liljeby, L., G. Astner, A. Bárány, H. Cedequist, H. Danared, S. Huldt, P. Hvelplund, A. Johnson, H. Knudsen, and K.-G. Rensfelt, 1986, Phys. Scr. **33**, 310.

Liljeby, L., and H. Danared, 1984, private communication.

McGuire, J. M., and L. Weaver, 1977, Phys. Rev. A **16**, 41.

McMaster, W. H., N. Kerr Del Grande, J. H. Mallett, and J. H. Hubbell, 1969, Compilation of X-Ray Cross Sections, UCRL-50174 Sec. II Rev. 1, Lawrence Radiation Laboratory, University of California, Livermore.

Mills, D. M., 1984, Physics Today **(April)**, 22.

Mowat, J. R., I. A. Sellin, D. J. Pegg, R. S. Peterson, M. D. Brown, and J. R. Macdonald, 1973, Phys. Rev. Lett. **26**, 1289.

Müller A., B. Schuch, W. Groh, E. Salzborn, H. F. Beyer, P. H. Mokler, and R. E. Olson, 1986, Phys. Rev. A **33**, 3010.

Niehaus, A., 1986, J. Phys. B **19**, 2925.

Nielson, E. H., L. H. Andersen, A. Bárány, H. Cederquist, P. Hvelplund, H. Knudsen, K. B. MacAdams, and J. Sorensen, 1984, J. Phys. B **17**, L139.

Olson, R. E., 1979, J. Phys. B **12**, 1843.

Paulus, T. J., 1985, IEEE Trans. on Nucl. Sci. **NS-32**, 1242.

Prior, M. H., R. Marrus, and C. R. Vane, 1983, Phys. Rev. A **28**, 141.

Rakavy G., and A. Ron, 1967, Phys. Rev. **159**, 50.

Richard, P., I. L. Morgan, T. Furuta, and D. Burch, 1969, Phys. Rev. Lett. **23**, 1009.

Robinson, M. T., 1970, Tables of Classical Scattering Integrals, ORNL-4556 UC-34 Physics, Oak Ridge National Laboratory, Oak Ridge, Tennessee.

Russek, A., 1963, Phys. Rev. **132**, 246.

Schlachter, A. S., W. Groh, A. Müller, H. F. Beyer, R. Mann, and R. E. Olson, 1982, Phys. Rev. A **26**, 1373.

Schmeissner, C., C. L. Cocke, and R. Mann, 1984, Phys. Rev. A **30**, 1661.

Schuch, R., et al., 1987, to be published.

Sellin, I. A., S. B. Elston, J. P. Forester, P. M. Griffin, D. J. Pegg, R. S. Peterson, R. S. Thoe, C. R. Vane, J. J. Wright, K.-O. Groeneveld, R. Laubert, and F. Chen, 1977, Phys. Lett. **61A**, 107.

Sellin, I. A., and D. J. Pegg, ed., 1975, Beam-Foil Spectroscopy, (Plenum Press, New York).

Short, R. T., C.-S. O, J. C. Levin, I. A. Sellin, B. M. Johnson, M. Meron, and K. Jones, 1987, Nucl. Instrum. Meth., to be published.

Short, R. T., C.-S. O, J. C. Levin, I. A. Sellin, L. Liljeby, S. Huldt, S.-E. Johansson, E. Nilsson, and D. A. Church, 1986, Phys. Rev. Lett. **56**, 2614.

Southworth, S., U. Becker, C. M. Truesdale, P. H. Korbin, D. W. Lindle, S. Owaki, and D. A. Shirley, 1983, Phys. Rev. A **28**, 261.

Tonuma, T., A. Yagishita, H. Shibata, T. Koizumi, T. Matsuo, K. Shima, T. Mukoyama, and H. Tawara, 1987, J. Phys. B **20**, L31.

Tseng, H. K., R. H. Pratt, Y. Simon, and R. Akiva, 1978, Phys. Rev. A **17**, 1061.

Ullrich, J., C. L. Cocke, S. Kelbch, R. Mann, P. Richard, and H. Schmidt-Böcking, 1984, J. Phys. B **17**, L785.

Ullrich, J., H. Schmidt-Böcking, S. Kelbch, C. L. Cocke, S. Hagmann, P. Richard, A. S. Schlachter, and R. Mann, 1987, Nucl. Instrum. Meth., to be published.

Vane, C. R., M. H. Prior, and R. Marrus, 1981, Phys. Rev. Lett. **46**, 107.

White, M. G., R. A. Rosenberg, G. Gabor, E. D. Poliakoff, G. Thorton, S. H. Southworth, and D. A. Shirley, 1979, Rev. Sci. Instrum. **50**, 1268.

Wiley, W. C., and I. H. McLaren, 1955, Rev. Sci. Instrum. **26**, 1150.

Wiza, J. L., 1979, Nucl. Instrum. Meth. **162**, 587.

Ziegler, J. F., J. P. Biersack, and U. Littmark, 1985, The Stopping and Range of Ions in Solids, (Pergamon Press).

APPENDICES

APPENDIX A

DERIVATION OF FLIGHT TIME EQUATIONS

Equations are derived below for calculations of ion flight times inside a TOF spectrometer using units which are convenient for experimental purposes. The flight time T_D for an ion with mass m and velocity v traversing a distance D is (in MKS units) $T_D = D/v$, or $T_D = D(m)^{1/2}/(2U)^{1/2}$, for kinetic energy $U = (mv^2/2)$. If the MKS units of D(m), m(kg), and U(J), are converted to the more convenient units D(cm), m(u), and U(eV), respectively, the flight time equation becomes

$$T_D(\text{in s}) = \frac{(1.67 \times 10^{-27}\ \text{kg/u})^{1/2}(10^{-2}\ \text{meters/cm})\ D(m)^{1/2}}{(1.60 \times 10^{-19}\ \text{C/e})^{1/2}\ (2U)^{1/2}} \qquad (A.1)$$

$$= (1.02 \times 10^{-6})\frac{D(m)^{1/2}}{(2U)^{1/2}}$$

$$T_D(\text{in } \mu\text{s}) = (1.02)\frac{D(m)^{1/2}}{(2U)^{1/2}}. \qquad (A.2)$$

An ion (m,q) accelerated by an electric field $\bar{E}$ for a time T attains a final velocity $\bar{v}$ (in MKS units)

$$\bar{v} = \frac{q\bar{E}}{m}\int_0^T dt = \frac{q\bar{E}T}{m} + \bar{v}_o. \qquad (A.3)$$

where $\bar{v}_o$ is the initial ion velocity. If only the one-dimensional case is examined, the vector signs may be omitted. The distance s the

ion travels in time T is

$$s = \int_0^T v\,dt = \frac{qET^2}{2m} + v_0T. \qquad (A.4)$$

The initial velocity can be expressed in terms of initial kinetic energy (U_0),

$$v_0 = \pm \frac{(2U_0)^{1/2}}{(m)^{1/2}} \qquad (A.5)$$

where the plus sign corresponds to initial velocities in the direction of the electric field, and the minus sign to velocities in the opposite direction. The following expression is then obtained using Equations A.4 and A.5,

$$\frac{qET^2}{2m} \pm \frac{(2U_0)^{1/2}T}{(m)^{1/2}} - s = 0. \qquad (A.6)$$

Equation A.6 can be solved for T using the quadratic formula,

$$T = \frac{m}{qE}\left[\mp (2U_0/m) + (2U_0/m + 2qsE/m)^{1/2} \right] \qquad (A.7)$$

where only the positive value of the second term has been kept, since T is a positive quantity. Equation A.7 simplifies to give

$$T = (1.02)\frac{(2m)^{1/2}}{qE}\left[(U_0 + qsE)^{1/2} \mp (U_0)^{1/2} \right] \qquad (A.8)$$

in the units u, e, eV, cm, and V/cm, as in Equation A.2. Now the minus sign corresponds to initial velocities in the direction of the electric field, and the plus to velocities in the opposite direction. Therefore, ion flight times in each region of a TOF spectrometer can be expressed in the form of Equation A.2 for field free regions, and Equation A.8 for regions with electric fields. The plus sign in Equation A.8 is only used for the source field region, since ions entering all other regions have velocities in the same direction as the electric fields.

An ion with an initial energy U_o, and velocity opposite to that of the electric field (E_s) in which it is born, will be turned around by the electric field and return to initial position acquiring the same U_o, but will have a velocity opposite its initial one. The time it takes the ion to turn around and return to its initial position (ΔT_u) is twice the second term in Equation A.8 (since the term is added for ions originally headed in the opposite direction of the field, and subracted for ions originally headed in the same direction),

$$\Delta T_u = (1.02)\frac{2(2mU_o)^{1/2}}{qE_s}. \qquad (A.9)$$

Thus, an initial energy U_o will produce a spread in flight times proportional to $1/qE_s$.

APPENDIX B

PPAD AND BEAM CHARGE STATE ANALYSIS SYSTEM

The following pages are included with the permission of Hans-Peter Hülskötter. They are taken from his Diplomarbeit titled "Experiments Investigating Coincidence Between Convoy and Rydberg Electrons and Projectile Charge States in Ion-Solid Collisions", Institut für Kernphysik, Westf.-Wilhelms-Universität Münster, Fed. Rep. of Germany, 1985." The text and figures appear without change, and are included for the benefit of the reader. All credit for the apparatus design and the description herein is given to Hans-Peter Hülskötter.

III.2.4 Charge State Analyzer

There are two principal methods to separate fast moving ions according to their charge state: magnetic and electric field separation. The method described here is the electrostatic charge state analysis. The dimensions of the charge state analyzer used in our experiments are shown in Figure III.9.

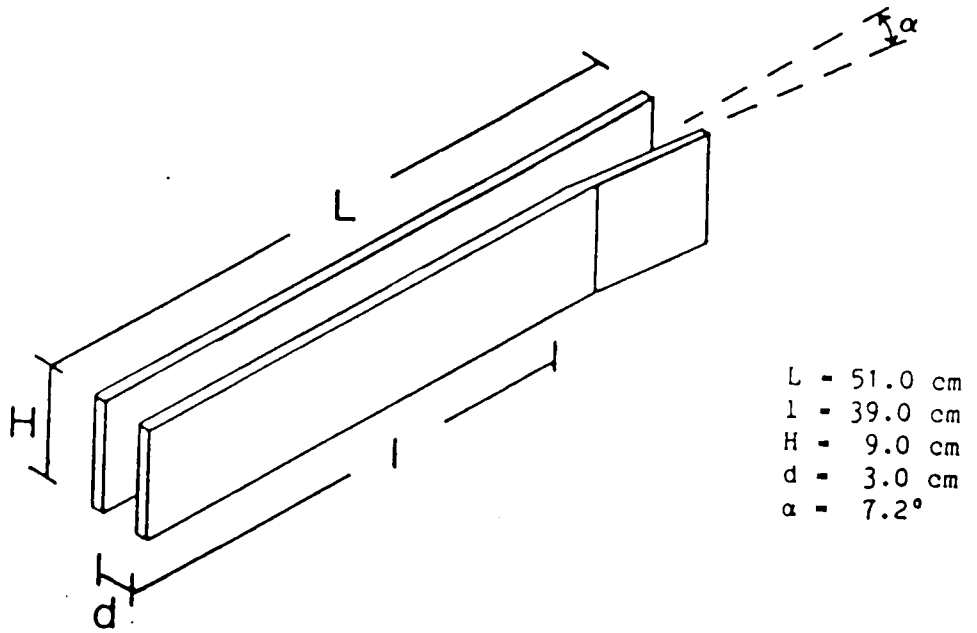


Figure III.9. Schematic diagram of electrostatic charge state analyzer

The ion beam enters the field region at ground potential at a distance of 1 cm from the flat plate. Not choosing the ground potential at the center between the two plates allows larger deflection angles for the ions. The flat plate has a positive potential, one-third the magnitude of the negative potential applied to the bent plate. Potential

differences of up to 40 kV can be applied between the plates without causing sparks (vacuum: 10^{-6} Torr). The voltages which are actually needed for the separation of ions with MeV/u energies are on the order of 20-30 kV. The total deflection s from the incident beam direction is given by:

$$s = 10^{-3}/4 \cdot q/A \cdot V/E \cdot (l_1^2/d_1 + l_2^2/d_2 + 2l_1l_2/d_1 + 2l_1l_3/d_1 + 2l_2l_3/d_2) \quad \text{(cm)} \qquad \text{(III.13)}$$

V: voltage in kV

E: beam energy in MeV/amu

q: ion charge

A: nuclear mass number

l_1: length of straight section (39 cm)

l_2: length of bended section (12 cm)

l_3: distance between charge state analyzer and ion detector (55 cm)

d_1: separation of the parallel plates (3 cm)

d_2: maximum separation of the bent plates (4.5 cm)

The bent part has been approximated by a second set of parallel plates with the separation of 3.75 cm. For our experimental setup Equation III.13 gives:

$$s \equiv 2/3 \cdot q/A \cdot V/E \quad \text{(cm)} \qquad \text{(III.14)}$$

III.2.5 Faraday Cup

In our beam line the Faraday cup has two functions:

- to monitor the beam current if the charge state analyzer is not used, and
- to screen out certain charge states if the charge state analyzer is used.

There are two apertures in front of the Faraday cup. The first one is grounded and has a diameter of approximately 20 cm, thereby shielding the plexiglass parts which are used to support the cup. The second aperture is connected to an electrical feedthrough so that a bias voltage can be applied. The cup itself is an aluminum cylinder, 30 cm long and 10 cm in diameter. Its back contains a movable aperture, as shown in Figure III.10. If the aperture is completely closed it serves as an ordinary Faraday cup. If the charge state analyzer is used, charge states which should not enter the ion detector can be screened out with this aperture.

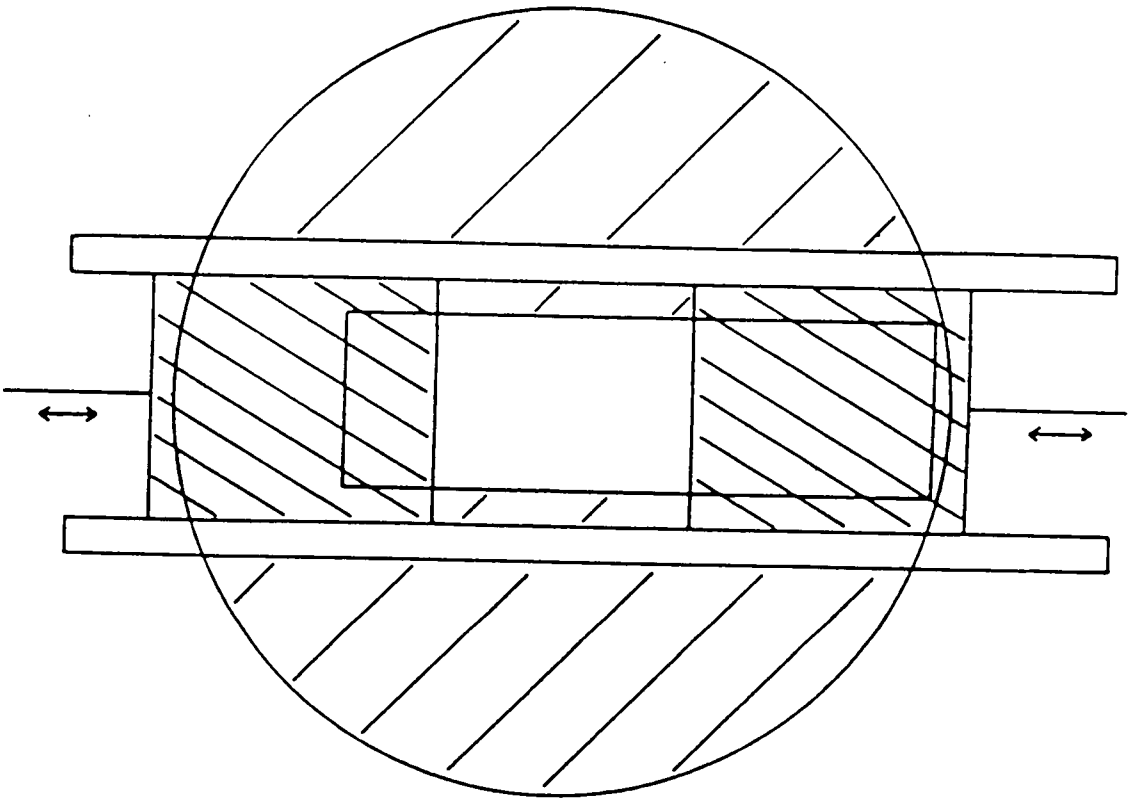


Figure III.10. Schematic diagram of aperture arrangement in the back of the Faraday cup.

III.2.6 Parallel Plate Avalanche Detector

The parallel plate avalanche detector[25] (PPAD) was provided by Schmidt-Böcking et al., Universität Frankfurt, FRG. A schematic view of the detector is shown in Figure III.11. The PPAD consists of two flat parallel electrodes. The upstream one is a highly transparent mesh which is usually held at ground potential. The second electrode is a copper-coated epoxy plate which has a position-sensitive pattern suitable for the experimental application.

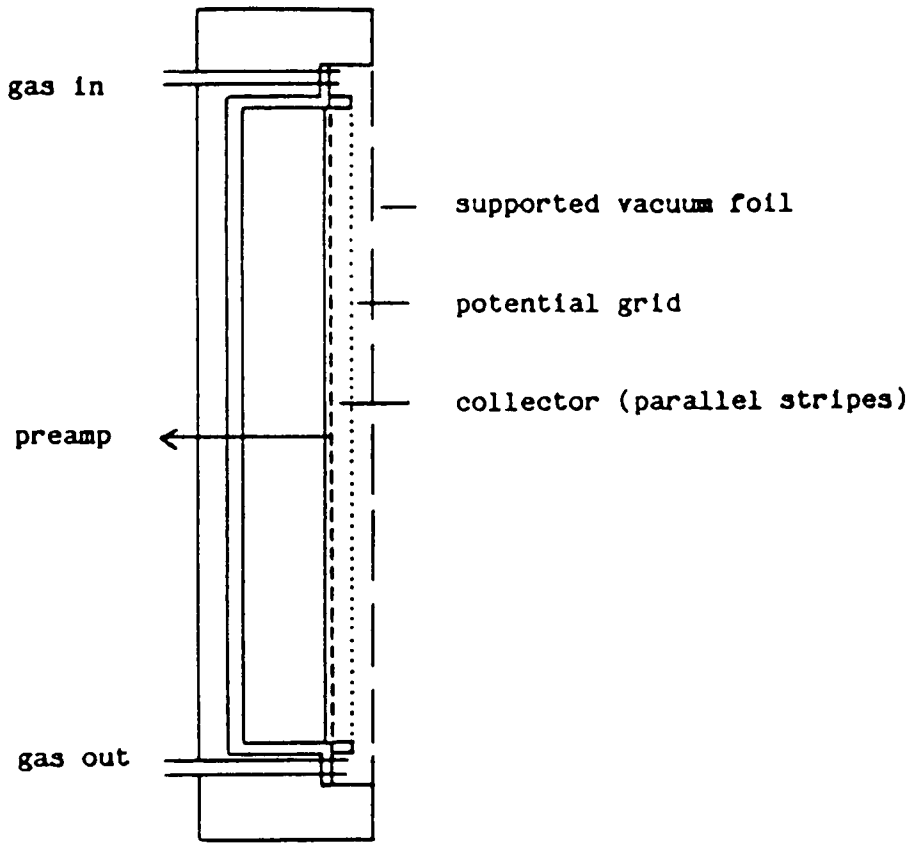


Figure III.11. Schematic diagram of parallel plate avalanche detector

In our experiments the electrode has thirty-two parallel stripes. To each of them a positive high voltage can be applied through a load resistor of approximately 100 kΩ. The volume between the two electrodes is filled with a counting gas (isobutane). Energetic particles (e.g., ions) which have entered the detector produce electron-ion pairs along their trajectories. Due to the potential difference between the electrodes the electrons gain enough kinetic energy to produce additional electron-ion pairs causing a Townsend-avalanche. Typical amplification factors are of the order 10^7 to 10^8. These avalanches cause fast potential changes at the collector stripes.

These signals are coupled out via a capacitor of approximately 10 nF and fed into fast preamplifiers. The output signals are sent through constant fraction discriminators before they are used for coincidence measurements. A vacuum foil is necessary to isolate the gas-filled detector volume from the high vacuum of the beam line. The detector is capable of count rates up to 10^6 counts per second. The average count rate in our experiment is 10^4-10^5 counts per second.

VITA

Robert Timothy Short was born in Tallahassee, Florida on May 20, 1956. He attended elementary schools in that city and was graduated from the Florida State University Developomental Research School (Florida High School) in June 1974. The following August he entered The University of North Carolina--Chapel Hill and completed two years in the General College there. In September 1976 he entered Florida State University in Tallahassee, and in June 1979 he received a Bachelor of Science degree in Physics.

In July 1979 he began work as a test engineer for Rockwell International at the Kennedy Space Center in Florida. He continued this work through the first four Space Shuttle launches, and in September 1982 entered The Graduate School of The University of Tennessee, Knoxville. Since that time, he has worked on the Doctor of Philoshophy degree with a major in Physics under the supervision of Professor Ivan A. Sellin, within the University of Tennessee Atomic Physics Group. The major emphasis of his work has been the study of ion-atom collsions and the interaction of synchrotron radiation with atoms and molecules.

The author is a memeber of Sigma Pi Sigma and The American Physical Society. Mr. Short will have a post-doctoral position at the Research Institute of Physics (Atomfysik) in Stockholm, Sweden after graduation.